REVIEW

Localised strain and doping of 2D materials

Frank Lee, [ID] *†[a] Manoj Tripathi, [ID] *†[a] Roque Sanchez Salas, [ID] [a] Sean P. Ogilvie, [ID] [a] Aline Amorim Graf, [ID] [a] Izabela Jurewicz[b] and Alan B. Dalton [ID] *[a]

There is a growing interest in 2D materials-based devices as the replacement for established materials, such as silicon and metal oxides in microelectronics and sensing, respectively. However, the atomically thin nature of 2D materials makes them susceptible to slight variations caused by their immediate environment, inducing doping and strain, which can vary between, and even microscopically within, devices. One of the misapprehensions for using 2D materials is the consideration of unanimous intrinsic properties over different support surfaces. The interfacial interaction, intrinsic structural disorder and external strain modulate the properties of 2D materials and govern the device performance. The understanding, measurement and control of these factors are thus one of the significant challenges for the adoption of 2D materials in industrial electronics, sensing, and polymer composites. This topical review provides a comprehensive overview of the effect of strain-induced lattice deformation and its relationship with physical and electronic properties. Using the example of graphene and MoS_2 (as the prototypical 2D semiconductor), we rationalise the importance of scanning probe techniques and Raman spectroscopy to elucidate strain and doping in 2D materials. These effects can be directly and accurately characterised through Raman shifts in a non-destructive manner. A generalised model has been presented that deconvolutes the intertwined relationship between strain and doping in graphene and MoS_2 that could apply to other members of the 2D materials family. The emerging field of straintronics is presented, where the controlled application of strain over 2D materials induces tuneable physical and electronic properties. These perspectives highlight practical considerations for strain engineering and related microelectromechanical applications.

1. Fundamentals of strain and doping

1.1. Susceptibility of 2D materials for strain and doping

The isolation of graphene in 2004 unleashed the veracity of thermodynamic stability in two-dimensional (2D) materials. One of the plausible explanations for their existence in the real world as 2D crystals is due to the rearrangements of atoms through structural distortions such as gentle crumbling or stretching.[26] However, these distortions influence the electronic properties and often alter the energy band gap.[32] For example, the physical deposition of 2D materials over a substrate of certain roughness and dielectric constant can lead to super-lubricious contact,[36] regulated out-of-plane deformation,[38] pseudo-magnetic field[39] or confinement effects,[40] depending on the type of the interfacial interactions (van der Waals, ionic or covalent).[41] The surface atoms of 2D materials are also directly exposed to the local environment such as air-borne impurities, chemical analytes and substrates, and are thus susceptible to mechanical strain, doping and/or strain-induced doping.[14] Therefore, these structural distortions and the influence of the surroundings play a crucial role to govern their localised physical and electronic characteristics.

Graphene is considered an ideal prototypical example of an atomic 2D system due to the combination of extreme elastic deformability (up to 25%),[42] high room-temperature charge mobility (μ = 15 000 cm^2 V^{-1} s^{-1}), and linear energy–momentum dispersion relation at Dirac point.[26] Graphene is sensitive towards its host surface that serves as a support; even a cleaned silica substrate with minimal roughness (in picometers) and trapped charges in the oxide layer exhibits high electron–hole charge puddles to graphene under a strain variation comparable to the length scale that causes localised charge fluctuations leading to variation in the energy of the Dirac point.[43] These unique features make graphene an excellent candidate to study pivotal aspects of strain such as deformed lattice-induced band-gap engineering, superconducting phenomena, topotronics and straintronics.[1,44] Moreover, the endeavour of graphene research encourages the exploration of other 2D families such as group-VI transition

[a]*University of Sussex, Brighton, BN1 9RH, UK. E-mail: frank.lee@sussex.ac.uk, m.tripathi@sussex.ac.uk, a.b.dalton@sussex.ac.uk*

[b]*University of Surrey, Guildford, GU2 7XH, UK*

†Authors contributed equally.

metal dichalcogenides (TMDs), MXenes, 2D perovskite,[45] 2D-Xenes (X = Si, Ge, Sn) and so on.[46]

This review highlights the intertwined relationship between strain and doping in 2D materials that need to be deconvoluted for their individual contribution. Here we focus on different structural modulation and interfacial interactions of graphene and other 2D materials (MoS$_2$, *etc.*) that lead to their strain and doping. The emphasis will be dedicated to the physics of charge transport associated with structural modification. The distribution of strain and doping will be covered through scanning probe techniques and Raman spectroscopy. Finally, we will discuss the integration of strain and doping into mainstream technologies for future applications in solid-state devices and sensing applications.

1.2. Influence of strain on graphene

The effect of strain on the electronic properties can be envisioned through distortion in the lattice structure. In graphene, carbon atoms are hexagonally arranged with two carbon atoms per unit cell (Fig. 1a).[20] The lattice basis is defined by vectors $\overrightarrow{a_1}$ and $\overrightarrow{a_2}$ where $|\overrightarrow{a_1}| = |\overrightarrow{a_2}| = a_0(3/2 \pm \sqrt{3}/2)$ and a_0 is the carbon–carbon separation of 0.14 nm. The straining of graphene affects its lattice vector and its associated electronic band structure. The three-dimensional point group of a gra-

phene crystal is D_{6h}.[44] It has been observed that under hydrostatic strain for deformation up to 15%, no such significant change in D_{6h} ($6/mm$) symmetry appears in the hexagonal lattice apart from pseudo gaps at G and M points, but Dirac point (DP) is clamped to the K point (Fig. 1b). Nevertheless, non-hydrostatic strain such as uniaxial strain lowers the symmetry of the graphene lattice associated to sixfold and threefold rotational symmetries. There is a transition from hexagonal D_{6h} ($6/mm$) to rhombic D_{2h} (mmm); also, the triangular shape Brillouin Zone (BZ) is converted into a polygon, as shown in Fig. 1c and d. The pseudo gap between K and K′ increases under the effect of strain for both armchair and zigzag configuration. Accordingly, the DP is also shifted from high-symmetry points within the BZ. Under the effect of shear strain, graphene lattice symmetry is transformed to monoclinic, a further lower symmetry class associated to symmetry group $2/m$. It has been observed that shear strain causes band gap opening in the graphene far enough from the failure strain.[14] Thus, modulation in the electronic band is possible without compromising the mechanical stability of graphene through shear straining (Fig. 1e).[20] These effects are investigated through phonon dispersion of graphene through acoustic phonon modes (A) and optical phonon modes (O) of graphene unit cell. The combination of these phonon modes is
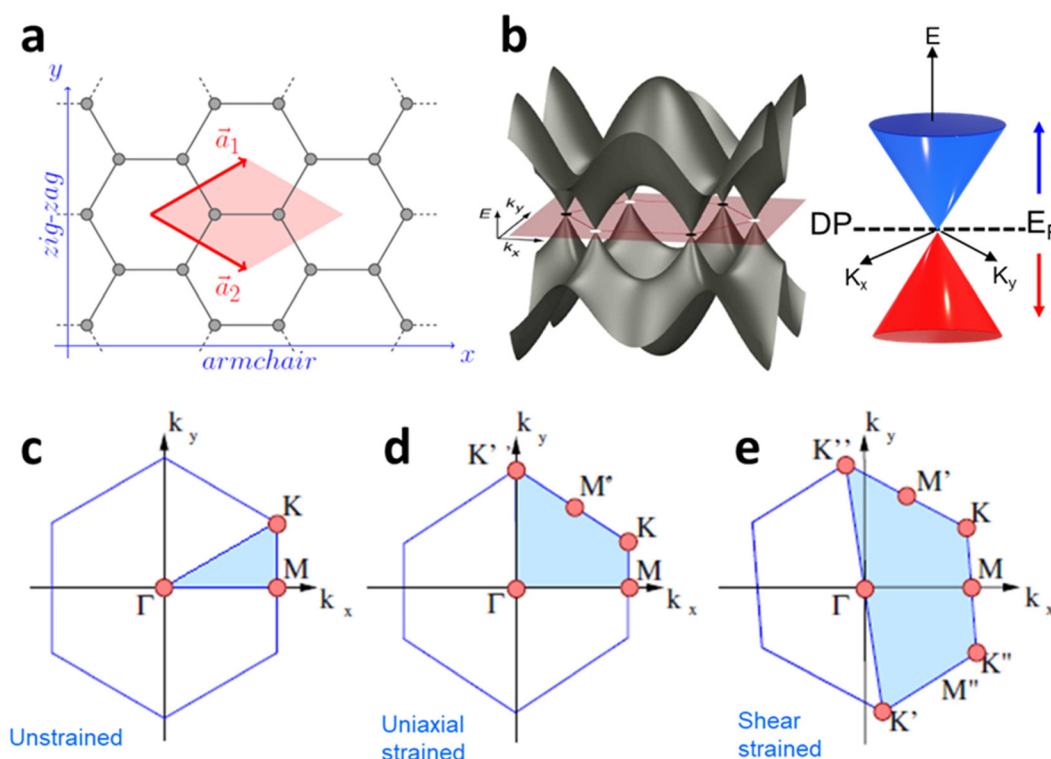

Fig. 1 (a) Hexagonal arrangement of carbon atoms in graphene, with vector basis $\overrightarrow{a_1}$ and $\overrightarrow{a_2}$. The shaded area represents the unit cell. The inequal crystallographic direction armchair along *x*-axis and zigzag along *y*-axis. (b) The high-symmetry (K) points of the hexagonal Brillouin zone (G, M, K) with a representation of characteristic linear bands intersecting at the Dirac point (DP) overlapped with Fermi energy level (E_F) for unstrained and doped graphene. The shift of E_F either to n or p leads to n-type and p-type doping respectively. Reprinted with permission from ref. 12 Copyright (2022) from IOP Publishing. (c–e) Illustration of BZ of graphene under strain. Reprinted with permission from ref. 20 Copyright (2022) from American Physical Society.

useful to evaluate the out-of-plane and in-plane vibration of the carbon atoms through Raman scattering.[47]

1.3. Influence of strain in MoS_2

The physical distortion in MoS_2 and other TMDs induces extrinsic disorder mostly after deposition over the substrate due to its intrinsic roughness and interfacial interaction such as ionic, covalent, electrovalent, van der Waals (vdW), *etc*.[36] The roughness of the substrate is an inherent factor that inevitably leads to localised bending of the flexible 2D materials. Unlike the atomic layer of graphene, 1L MoS_2 has three atomic layers (S–Mo–S) and exhibits a significant alternation in electronic structure that causes charge fluctuations during localised bending;[23] see schematic in Fig. 2a and b. The electronic band structure dispersion over a supported substrate exhibits a deviation from its strain-free suspended membrane, where in the former, large broadening of electronic band structures along the energy axis has been observed.[23] The local corrugation of MoS_2 over silica substrate (*i.e.*, vdW interaction) is reported to cause band gap (E_g) widening up to 2.65 eV without any aid of external straining. During the bent state, the spatial distribution of the S-atoms is altered. The atomic distances between the S-atoms increases in the inner (or outer) and decreases (or inner) in the sulphur layer; see Fig. 2c and d. The effect of these morphological corrugations is monitored through scanning tunnelling microscopy (STM) and correlated with localised variation with the E_g in Fig. 2d. It has been observed that there is a direct correlation with the conformation of MoS_2 and its difference in the conduction band minimum (CBM) and valence band maximum (VBM) shows strain induced E_g modulation.[13] The relation between the radius of curvature of the bent MoS_2, induced strain and its

variations in the E_g is illustrated in Fig. 2e, where a power law relationship is identified between band gap and radius of curvature, which is also related to the transformation of the direct to indirect band gap with increasing strain. This intrinsic corrugation-induced bending has converted 80% area of 1L MoS_2 into the indirect band (around strain 1.5%) which is also reflected in the reduction of photoluminescence (PL) intensity. It has been observed that the strain values lying between 0.47–0.62% are responsible for the direct band gap, while 1.0–1.2% strain is responsible for indirect transition (Fig. 2f). The localised spatial distribution of indirect (dark blue colour) and direct (red colour) band gap along with local bending strain contour plot for MoS_2-silica system is presented in Fig. 2g.[13] The modulation of band gap due to physical strain is also regulated to texture designed surfaces. It has been observed that a strain up to 2.4% can alter the optical band gap around 108 meV.[48] Over a textured surface such as nanocones, the externally induced strain can be reached up to 3% that leads to the band gap reduction up to 0.46 eV.[49]

1.4. Gate doping and chemical doping

In the modern-day electronics, it is imperative to understand the modulation in electronic properties of the material through external stimulating environment. The injection of the charge carriers, either electrons, holes or ions to 2D materials can be performed through an electric field, electrochemical doping or chemical treatment without altering the physical properties.[10] Generally, the electric field doping is carried out through field effect transistors (FET) with changing conducting channels between the mounted 2D material and applied gate voltage (V_g). A positive V_g injects electrons, while negative V_g induces higher density of holes in the 2D material,
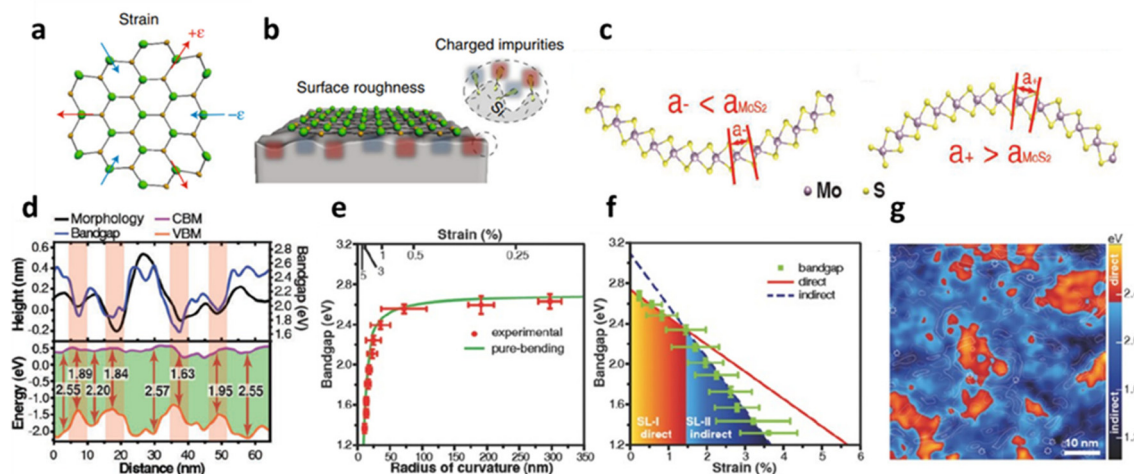

Fig. 2 Substrate induced strain in MoS_2: (a) schematic illustration of 1L MoS_2 with compressive and tensile strain. (b) Localised bending curvature from substrate roughness. (c) The conformation-induced bending curvature influences the separation distance between the inner and outer layers of sulphur atoms in atomic MoS_2. (d) STM line profile of MoS_2 topography and its associated band gap variations. (e) The relation between strain induced from morphology and radius of curvature of a bent MoS_2 with band gap. (f) Transformation of direct to indirect transition band gap at different strain values. Reprinted with permission from ref. 13 Copyright (2022) from John Wiley and Sons. (g) Spatial distribution of localised region showing indirect and direct transition of the band gap. Reprinted with permission from ref. 23 Copyright (2022) from Springer Nature.

consequently altering the electric current. The relation between the surface charge density n and applied voltage V_g is illustrated in eqn (1):

$$n = \varepsilon_0 \varepsilon \frac{V_g}{t} e \qquad (1)$$

where, ε_0 and ε are the permittivity of free space and the supported substrate respectively, t is the thickness of the supported substrate oxide layer (e.g., silica), and e is the electron charge. The coefficient of the surface charge density induced by field effect, n/V_g, is estimated as 7.2×10^{10} cm^{-2} V^{-1}. The change in carrier concentration shifts the Fermi energy (E_F) of the 2D material accordingly. For monocrystalline graphene, E_F of holes and electrons has been observed to be directly proportional to their concentrations ($E_F \propto n$), which is qualitatively different to its 3D bulk structure ($E_F \propto n^{2/3}$).[50] Under pristine conditions, graphene conductivity (σ) also increases linearly with V_g for both injections of electrons and hole carriers. The carrier mobility ($\mu = \sigma/ne$) has been measured up to 15 000 cm^2 V^{-1} s^{-1} for both carriers independent of temperature range between 10–100 K.[16]

The electronic doping of graphene can also be carried out through adsorbate deposition of different electron affinities. Surface dopant with higher work function than the host material, such as metal oxides and oxidising gases (e.g., MoO$_3$, NO$_2$), causes p-type doping, while the surface dopant of lower work function, named as alkali metals and gases rich in electron pair (e.g., NH$_3$), are responsible for the donation of electrons and causes n-doping. This phenomenon at the molecular scale can be explained through direct surface charge exchange across the electrochemical potential gradient at the interface between the 2D materials and surface dopant, which corresponds to the relative position of graphene E_F and the molecular orbital level of surface dopants. If graphene E_F is higher than the energy level of lowest unoccupied molecular orbital (LUMO) of an adsorbate, the electron will flow from graphene to the adsorbate, making graphene p-type doped. If the E_F of graphene is lower than the level of highest unoccupied molecular orbital (HOMO), graphene gains the electron and becomes n-type doped (Fig. 3a).[3] In semiconductors (e.g., metal dichalcogenides) with finite E_g, the energy level of valence band, conduction band and E_F relative to LUMO/HOMO of the adsorbate molecule determine the type of doping to reach thermal equilibrium. If VBM of the semiconductor lies above the lowest level of LUMO, the electron will be transferred from the valence band to the adsorbate during contact. This charge migration changes the electron density at the interfaces which lead to band bending in upward direction and hole accumulation at the semiconductor, causing p-type doping. Nevertheless, if the CBM of the semiconductor lies slightly lower than the highest occupied HOMO level before contact, the electron will transfer from HOMO of the adsorbate to the conduction band of the semiconductor. It causes downward band bending and higher accumulation of the electrons in the semiconductor (n-type doping) until the stage of thermal equilibrium is reached (Fig. 3b).

1.5. Influence of doping on conductivity

The electrical doping, either by electric field or surface adsorbate leads to alteration in current. Quantively, the electrical conductivity σ and carrier concentration n can be related by $\sigma \propto n^a$, where $a < 1$ for charge impurities and $a > 1$ for structural distortion such as ripples. Fig. 4a–c shows an example of graphene-based FET device demonstrating the change in conductivity from its pristine state to adsorbed impurities (K-atoms
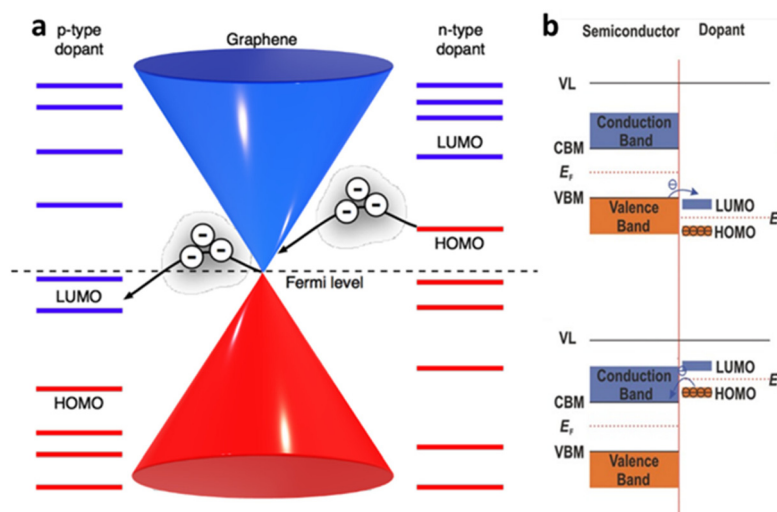

Fig. 3 Charge transfer mechanism between 2D materials and surface dopant: (a) schematic diagram of the energy bands of graphene with different electron affinities of the dopant. Reprinted with permission from ref. 3 Copyright (2022) from Beilstein Journal of Nanotechnology. (b) Schematic band diagram of the semiconductor based 2D materials towards surface dopants. Reprinted with permission from ref. 17 Copyright (2022) from John Wiley and Sons.
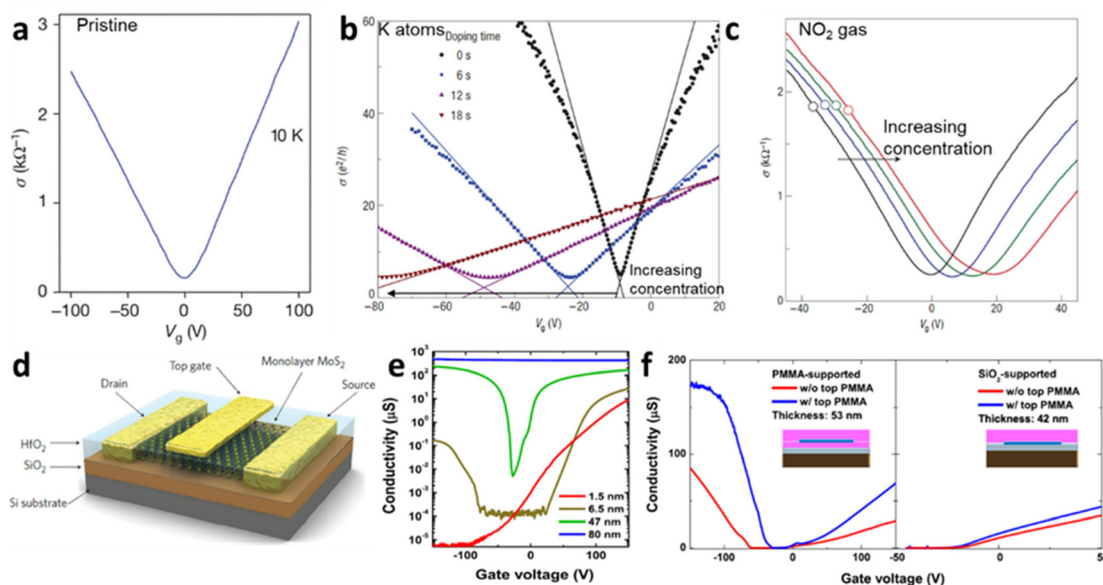
Fig. 4 Ambipolar transfer characteristics at different gate voltage (V_g) for (a) pristine graphene,[2] (b) potassium adsorbed graphene at different concentration added at different time interval[16] and (c) NO$_2$ doped graphene at different concentration.[27] Reprinted with permission from ref. 2, 16 and 27 Copyright (2022) from Springer Nature. (d) Schematic set-up of MoS$_2$ FET with top gate (dielectric). (e) Conductivity of MoS$_2$ as function of thickness from unipolar to ambipolar. (f) Conductivity of MoS$_2$ at different substrates (SiO$_2$ and PMMA). Reprinted with permission from ref. 33 Copyright (2022) from AIP Publishing.

and NO$_2$ gases) for different concentrations. It has been observed that the minimum conductivity with increasing the concentration of impurities (such as potassium atoms) saturates to a constant value around 4e^2/h (for h as Planck constant) for graphene.[2] Also, it leads to shifts in minimum V_g and is responsible for the asymmetry in the conductive curves for different polarities due to the change in the dopant concentration. The slope of the conductivity curve $\sigma(V_g)$ unravels the measure of impurity scattering (so called field-effect mobility; $\mu = \Delta\sigma/\Delta ne$). Thus, the deviation in the slope values indicates that the doping from the impurities influences the scattering rate as observed in Fig. 4b for K-atoms and in Fig. 4c for NO$_2$ adsorption.

Unlike graphene as zero-gap semi-metal, single layer of TMD, such as molybdenum disulphide (MoS$_2$), have a wide band gap ($E_g \gg 1.8$ eV) which is useful for monitoring electronic doping with reasonable high mobilities ~217 cm^2 V^{-1} s^{-1} (and >500 cm^2 V^{-1} s^{-1} for bulk).[51] The mobility of MoS$_2$ varies with its thickness, which is related to the long-range dielectric effect and the dominance of long-range disorder that minimises the scattering of charges (Fig. 4d and e). The mobility of the charges in MoS$_2$ can also be modulated through the addition of the superstrate (sometimes top gate) with highly dielectric materials (HfO$_2$, ZrO$_2$ PMMA) (Fig. 4f).[33] The variation in the E_g of MoS$_2$ with the thickness (Fig. 4e) makes it interesting for nanoelectronics applications to replace silicon in complementary metal–oxide–semiconductor (CMOS) logic devices. It is ideal for a semiconductor with $E_g > 0.4$ eV to have a current on/off ratio (I_{on}/I_{off}) in the range between 10^4 and 10^7. While this value is limited in pristine graphene,[52] the

single crystal of MoS$_2$ has demonstrated $I_{on}/I_{off} > 10^6$ at an applied voltage of ±4 V comparable to silicon films.[53] As shown in Fig. 4e and f, the conductivity of MoS$_2$ varies with thickness and the nature of substrate; thinner layer (bi-layer) shows the n-type unipolar behaviour mostly over the SiO$_2$ substrates. Nevertheless, MoS$_2$ displays ambipolar behaviour around 6 layers with lower mobility of holes than electrons. At bulk state (>50 nm), major carrier of holes has been reported, indicating the p-type operation, which is suitable for FET and sensing applications.[33] At similar thickness, dielectric polymeric support leads to the ambipolar trend in the conductivity, compared to unipolar trend over the SiO$_2$ substrates with lower mobility. It has been argued that the presence of short-range disorder, chemical interaction with silica, or interface roughness scattering play important roles to bring down the conductivity.[33]

1.6. Measuring doping through Raman spectroscopy

Raman spectroscopy is a non-destructive optical characterisation technique sensitive to changes in the lattice structure, the electronic states, and the energy band of several 2D materials. The Raman active modes of the 2D materials are strongly related to the coupling between electrons and phonons (Fig. 5a and b).[17] A shift in peak position (ω_G) in the Raman active peak from its charge neutral state indicates the altering conditions of carrier concentration. In graphene, the extra charge carriers residing in honeycomb lattice structure lead to dynamical perturbation of G mode (~1580 cm^{-1}) lattice vibration. During the Raman scattering process, there is a creation and annihilation of long-wavelength virtual electron–
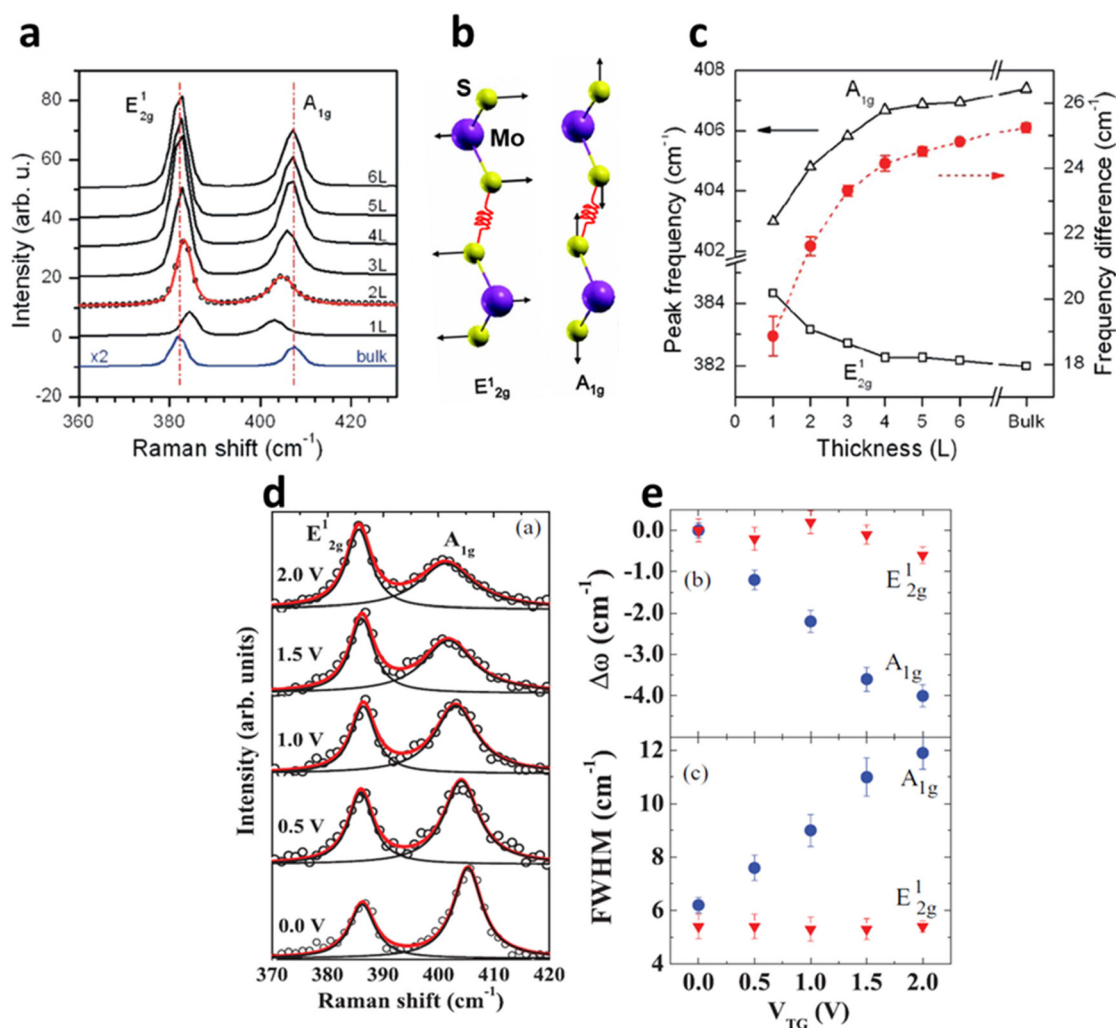
Fig. 5 (a) Raman spectrum of MoS$_2$ at a different number of layers . (b) The schematic illustration of S and Mo atoms vibrations for E$^1_{2g}$ and A$_{1g}$ phonon modes. Reprinted with permission from ref. 1 Copyright (2022) from American Physical Society. (c) The shift in the Raman modes of MoS$_2$ at different thicknesses. Reprinted with permission from ref. 15 Copyright (2022) from American Chemical Society. (d) The shift in the Raman modes and its broadening of 1L MoS$_2$ at different top-gate voltages (V). The Raman peaks are fitted with Lorentzian line fit to monitor the peak shift and its broadening. (e) The shift in peak positions ($D\omega$) and peak width (FWHM) of E$^1_{2g}$ and A$_{1g}$ at the gate voltage range 0–2 V. Reprinted with permission from ref. 28 Copyright (2022) from American Physical Society.

hole pair across the Dirac point.[54] The energy range of the virtual electron–hole pairs are regulated through Pauli principle, which is decided by E_F level. In undoped graphene, the onset energy ($\hbar\omega_G$) is considered zero. Under doped conditions, the increase/decrease in the carrier concentration improves the onset energy for vertical transition of an electron from a π valence band to a π* conduction band state to create virtual electron–hole pairs to $2E_F$ (under the limitation of Pauli principle). Thus, the rise/fall of onset energy conditions leads to upshift/downshift of the G mode of graphene.[17] At variable V_g, it has been observed G-peak position shift is minimum at the DP, indicating blue shift (stiffening) in G-peak position for both polarities. It is anticipated that the stiffening of the G mode is due to non-adiabatic removal of Kohn anomaly, which is usually responsible for phonon softening in graphitic

materials under the condition of strong electron–phonon interaction.[55]

Also, the width of G phonon (G_G) modes responds complimentarily to the stiffening of G mode. Yan and co-workers[21] observed the V_g dependence for both ω_G and G_G that exhibit symmetrical changes at V_g = 18 V (Fig. 5c). A similar trend has also been demonstrated by Das et al.[10] at V_g = 0.6 V which is directly related to the band structure of graphene as shown in Fig. 5d. The reduction in the G_G (15 cm^{-1} to 6.5 cm^{-1}) with increasing |V_g − V_{DP}| indicates longer phonon lifetime relating to electron and hole concentration. This trend has been understood as Landau damping of phonons at higher carrier concentration in which the mode decays into particle–hole pair.[21] At the 2D Raman modes (~2700 cm^{-1}) of graphene, the photoexcited electron emits an A$_{1g}$ phonon and the valley changes from K to K′ due to conservation
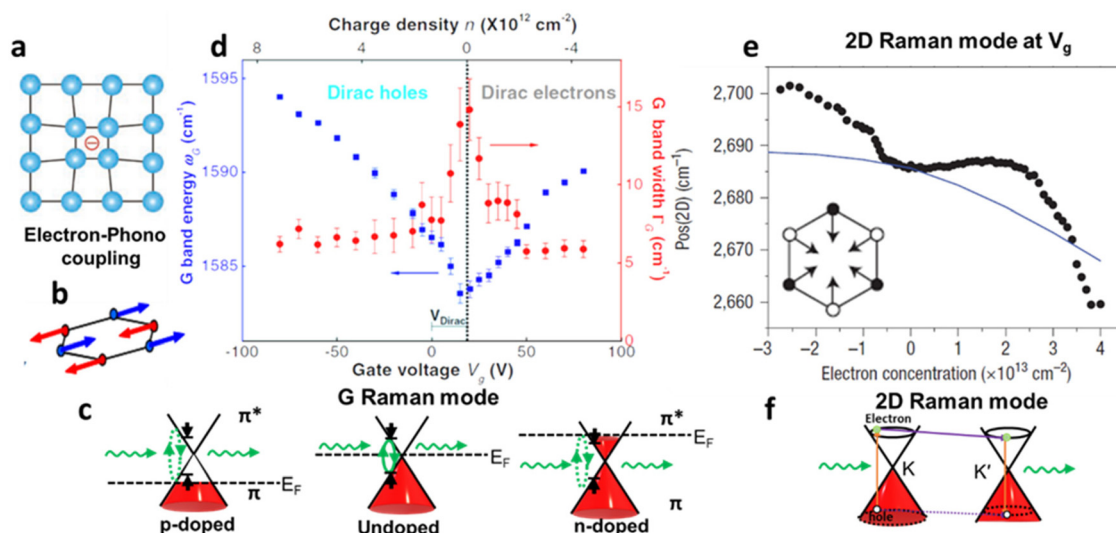
Fig. 6 Raman scattering of graphene: (a) schematic diagram of electron–phonon coupling. (b) G-phonon mode of vibrating carbon atoms. (c) Effect of G-peak position (ω_G) and G-peak width G_G at different V_g. Reprinted with permission from ref. 10 Copyright (2022) from Springer Nature. (d) Shift in 2D peak position ω_G at different carrier concentration induced from different V_g, inset showing the schematic diagram vibration of carbon bonds in 2D Raman mode. Reprinted with permission from ref. 21 Copyright (2022) from American Physical Society. (e) Schematic of a Raman process in Dirac cones of graphene G Raman mode and (f) 2D Raman mode. Reprinted with permission from ref. 17 Copyright (2022) from John Wiley and Sons.

of momentum. The effect of electronic doping of 2D Raman mode is different from G mode that electronic doping over 2D has minimal effect until a certain carrier concentration ($\sim 3 \times 10^{13}$ cm^{-2}) is achieved through the polymeric ionic layer at ~ 3 V. At higher V_g there is a redshift (softening), while for the hole doping there is a blue shift (Fig. 5e and f).[17]

Raman spectroscopy of semiconducting TMDs is also influenced by carrier doping determined by phonon characteristics. In MoS$_2$, the evolution of the zone centre of E$^1_{2g}$ and A$_{1g}$ is due to lateral displacement of Mo–S atoms in the basal plane and atomic sulphur vibration along the c-axis respectively (Fig. 6a and b). The layer dependent Raman studies of MoS$_2$ have shown the decrease in E$^1_{2g}$ frequency and increase in A$_{1g}$ phonons with increasing thickness (Fig. 6c). This opposite trend of E$^1_{2g}$ reflects the stacking induced structural change in the MoS$_2$, and its anomalous phenomenon is attributed to enhanced dielectric screening of long-range Coulomb interaction between the effective charges at higher thickness.[1] In 1L MoS$_2$, increasing concentration of electrons occupies the bottom of the conduction band at K point, which has the characteristics of d$_{z^2}$ of Mo.[28] This occupancy of the antibonding state in the conduction band enhances the total electronic energy of the system, resulting in weaker Mo–S bonds and phonon softening of A$_{1g}$ (red shift up to 4 cm^{-1}) Raman mode as illustrated in Fig. 6d and e. The out-of-plane A$_{1g}$ Raman mode preserves the symmetry of the system and has strong electron phonon coupling than E$^1_{2g}$, which explains the minor alteration (0.6 cm^{-1}) of E$^1_{2g}$ under biasing conditions. Similarly, G_{A1g} increases up to 6 cm^{-1} while G_{E12g} remains insensitive. The phonon softening of A$_{1g}$ MoS$_2$ at higher electron concentration has a distinctive trend than phonon hardening in graphene, as the latter blocks the generation of phonon induced electron–hole pair. Nevertheless, having a finite E_g, MoS$_2$ shows

different responses at various laser energy, especially at resonance excitation of laser energy used in the investigation.[56–58]

2. Deconvolution of strain and doping of 2D materials

2.1. Construction of strain and doping correlation

Unlike textured surfaces that induce static straining, soft surfaces such as polymeric materials allow dynamic strain and doping in 2D materials. Since Mohiuddin *et al.*[8] first reported the G and 2D peak position shifts due to applied uniaxial strain, comprehensive studies on Raman spectroscopy of graphene in response to mechanical stimulus had been carried out.[47] It is observed that the compression (tension) of the lattice reduces (increases) the interatomic distances and in turn leads to the redistribution of electronic charges, which upshifts (downshifts) the vibrational Raman modes.[47,59] Consider a general strain tensor

$$\varepsilon = \begin{pmatrix} \varepsilon^{ll} & \varepsilon^{lt} \\ \varepsilon^{tl} & \varepsilon^{tt} \end{pmatrix} \qquad (2)$$

where superscripts l and t represent the strain components in longitudinal and transverse directions, respectively. The rate of hydrostatic strain ($\varepsilon^h = \varepsilon^{ll} + \varepsilon^{tt}$) of Raman mode i (G or 2D) can be related by Grüneisen parameter as:[8,47]

$$\gamma_i = -\frac{1}{\omega_i^0} \frac{\partial \omega_i}{\partial \varepsilon^h} \qquad (3)$$

where ω_i is the Raman peak position, ω_i^0 is the strain-free Raman peak position, and γ_i is the Grüneisen parameter of the

corresponding Raman mode. For an applied uniaxial strain $\varepsilon^{\mathrm{uni}}$, the G peak splits into G^+ and G^- due to the non-zero shear component of the strain ($\varepsilon^{ll} \neq \varepsilon^{tt}$), while 2D peak does not split as it is associated with phonons at K point.[60,61] Given that $\varepsilon^{ll} = \varepsilon^{\mathrm{uni}}$ and $\varepsilon^{tt} = -\nu\varepsilon^{\mathrm{uni}}$ where ν is the Poisson's ratio of graphene, the Grüneisen parameter can then be expressed by:

$$\gamma_{\mathrm{G}}^{\mathrm{uni}} = -\frac{1}{\omega_{\mathrm{G}}^0}\frac{\Delta\omega_{G^+} + \Delta\omega_{G^-}}{2(1-\nu)\varepsilon^{\mathrm{uni}}} \tag{4}$$

$$\gamma_{2\mathrm{D}}^{\mathrm{uni}} = -\frac{1}{\omega_{2\mathrm{D}}^0}\frac{\Delta\omega_{2\mathrm{D}}}{(1-\nu)\varepsilon^{\mathrm{uni}}} \tag{5}$$

where $\Delta\omega$ is the Raman shift deviated from the no-strain point ω^0. When studying interactions between graphene and other 2D materials, however, biaxial strain $\varepsilon^{\mathrm{bi}}$ is usually involved.[14] In such case, $\varepsilon^{ll} = \varepsilon^{tt} = \varepsilon^{\mathrm{bi}}$ and G peak no longer splits due to the cancellation of shear deformation components; hence eqn (3) can be rewritten as:

$$\gamma_i^{\mathrm{bi}} = -\frac{1}{\omega_i^0}\frac{\Delta\omega_i}{2\varepsilon^{\mathrm{bi}}} \tag{6}$$

or,

$$\Delta\omega_i = -2\gamma_i\omega_i^0\varepsilon. \tag{7}$$

By applying the experimentally or theoretically determined value of γ_i,[8,62,63] one can deduce the strain distribution of graphene through Raman shifts measurement. At low strain regime ($\varepsilon < 0.5\%$), the phonon frequencies of both G and 2D vary linearly with strain.[8] Hence, γ_i is a defined constant which will be useful in the construction of a correlation plot that will be discussed in later sections.

Raman modes of graphene are also susceptible to carrier concentration n due to the modification of electron–phonon coupling,[10,64] which is generalised in Fig. 7a following results from Das and coworkers.[10] Both p-doping and n-doping upshift G mode owing to the removal of the Kohn anomalies at Γ point,[55] while an increase in carrier concentration (higher n-doping or less p-doping) always downshifts 2D mode due to the electronic transition of the energy of the phonons in double-resonant scattering.[10,54] As pristine graphene and hybrid systems thereof are usually p-doped,[35,65–67] it is expected the coordinates of Raman peak positions of unstrained graphene lie on the green coloured line in Fig. 7a. Low p-doping level (-1.0×10^{13} cm^{-2} <

$n < 0$) can be well approximated by a first-order polynomial in terms of G or 2D peak position; it is thus possible to introduce a doping coefficient k_i that:

$$\Delta\omega_i = k_i n \tag{8}$$

As k_i is already known from Fig. 7a, the carrier concentration of graphene can be computed by measuring its Raman shifts. The interaction between graphene and other 2D materials often leads to both mechanical and electrical modulation, and this combined effect of strain and doping on Raman shift can be formulated by summing up eqn (7) and (8):

$$\Delta\omega_i = -2\gamma_i\omega_i^0\varepsilon + k_i n \tag{9}$$

Lee and co-workers[67] were the first to separate the effect of strain and doping by noticing that ε and n are linearly independent. By keeping other external effects constant such as single calibrated laser wavelength for dispersive Raman modes (e.g. D and 2D modes in graphene) and constant low laser power to avoid laser-induced temperature change throughout different measurements,[68] $\Delta\omega_{\mathrm{G}} - \Delta\omega_{2\mathrm{D}}$ space can be regarded as a linear transformation of ε–n space, and each coordinate of Raman peak position represent a unique strain and doping configuration, i.e.,

$$\begin{pmatrix}\Delta\omega_1 \\ \Delta\omega_2\end{pmatrix} = T\begin{pmatrix}\varepsilon \\ n\end{pmatrix} \tag{10}$$

where

$$T = \begin{pmatrix} -2\gamma_1\omega_1^0 & k_1 \\ -2\gamma_2\omega_2^0 & k_2 \end{pmatrix} \tag{11}$$

In graphene system, ω_1 and ω_2 correspond to G and 2D modes respectively. A correlation plot can therefore be drawn in Fig. 7b with contour lines representing isostrain and isodoping. The value of strain and doping can then be evaluated by an inverse transformation:

$$\begin{pmatrix}\varepsilon \\ n\end{pmatrix} = T^{-1}\begin{pmatrix}\Delta\omega_1 \\ \Delta\omega_2\end{pmatrix}$$
$$= \frac{1}{-2\gamma_1\omega_1^0 k_2 + 2\gamma_2\omega_2^0 k_1}\begin{pmatrix} k_2 & -k_1 \\ 2\gamma_2\omega_2^0 & -2\gamma_1\omega_1^0 \end{pmatrix}\begin{pmatrix}\Delta\omega_1 \\ \Delta\omega_2\end{pmatrix} \tag{12}$$

Using this equation, we can measure two Raman shifts, G and 2D for graphene, to determine two quantities of strain
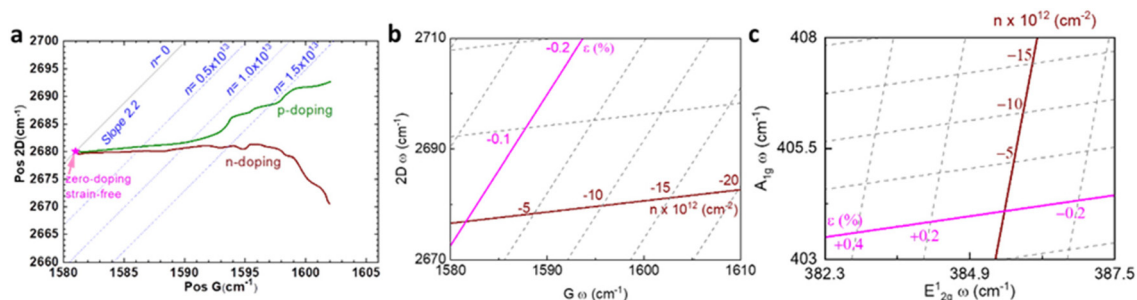

Fig. 7 Illustration of strain and doping correlation plot (Pos G vs. Pos 2D) of (a) graphene for both p- and n-doping, (b) graphene for only p-doping, and (c) MoS$_2$. Each Raman dataset in G-2D axes represent the corresponding strain and doping in ε–n axes.

and doping. The sets of eqn (7)–(12) are not only applicable to graphene, but also to other 2D materials, such as MoS_2, where subscripts (1) and (2) represent E^1_{2g} and A_{1g} modes respectively.[69] Straining MoS_2 leads to the modification of carrier effective masses and band gap energy,[48,70] which consequently shifts the phonon frequencies of E^1_{2g} and A_{1g} modes. On the other hand, doping MoS_2 results in the occupation of anti-bonding states at the K point,[28,69] which results in downshifts of both E^1_{2g} and A_{1g} modes. Therefore, with Grüneisen parameters γ_i and doping coefficients k_i of E^1_{2g} and A_{1g} modes known, we can also construct an analogous correlation plot of MoS_2 to decouple strain and doping (Fig. 7c).

2.2. Determination of Grüneisen parameters and doping coefficients of 2D materials

Grüneisen parameters of graphene can be characterised either experimentally or theoretically by various techniques. At uniaxial strain, a typical method would be depositing graphene on a flexible substrate such as polyethylene terephthalate (PET) and bending the substrate (Fig. 8a).[8] Assuming graphene is adhered to the substrate, this induces strain on graphene, which leads to Raman peak shifting (Fig. 8b). Grüneisen parameters can then be deduced by linear fitting of peak positions using eqn 4 and 5. Alternatively, pressure-induced compressive strain leading to shifts of graphene Raman peaks also enables the calculation of Grüneisen parameters.[71] Several empirical methods for Grüneisen parameters at biaxial strain have also been developed, including piezoelectric actuator,[72] nanobubble curvature,[73] shallow depression on patterned SiO_2,[74] and recently, substrate-induced strain by thermal expansion coefficient (TEC) mismatch.[75] Theoretically, Grüneisen parameters can also be deduced by DFT and first-principles calculations,[8] which agree well with experimental values. Similarly, Grüneisen parameters of TMDs at uniaxial strain are measured by depositing it on polymers with subsequent bending[48,70] as

well as density functional theory with first-principles calculations.[76] Michail et al.[22] lately introduced in situ determination of Grüneisen parameters of MoS_2 at biaxial strain using flexible cruciform substrate (Fig. 8c) backed by DFT calculations, which is essential for the evaluation of localised strain in 2D materials. Values of the above parameters of graphene and MoS_2 are listed in Tables 1 and 2 respectively.

Measurement of doping coefficients can be obtained directly by electronic top-gated field-effect transistor[10,28] discussed in the previous section. An applied top-gated voltage contributes to a change in the doping concentration of 2D materials, which can be monitored by Raman spectroscopy. Generally accepted values of doping coefficients are respectively $k_G = -1.407 \times 10^{-12}$ cm^{-1}, $k_{2D} = -0.285 \times 10^{-12}$ cm^{-1},[10] $k_{E^1_{2g}} = -0.33 \times 10^{-13}$ cm^{-1} and $k_{A_{1g}} = -2.22 \times 10^{-13}$ cm^{-1}.[28]

Table 1 Determination of Grüneisen parameters of graphene

γ_G	γ_{2D}	Strain	Method	Ref.
1.99	2.7	Uniaxial	Experimental	71
1.99	3.55	Uniaxial	Experimental	8
1.87	2.7	Uniaxial	Theoretical	8
1.8	2.6	Biaxial	Experimental	73
1.8	2.8	Biaxial	Experimental	72
1.95	3.15	Biaxial	Experimental	75
2.4	3.8	Biaxial	Experimental	74
1.8	2.7	Biaxial	Theoretical	8

Table 2 Determination of Grüneisen parameters of MoS_2

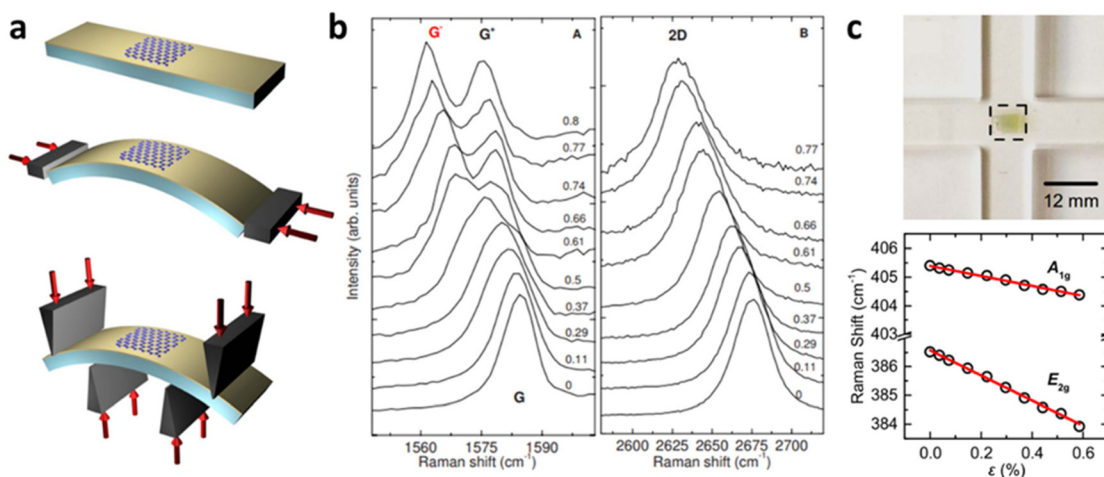| $\gamma_{E_{2G}^1}$	$\gamma_{A_{1G}}$	Strain	Method	Ref.
0.6	0	Uniaxial	Experimental	70
1.1	0	Uniaxial	Experimental	48
0.65	0.21	Uniaxial	Theoretical	76
0.6	0.22	Biaxial	Experimental	22
0.56	0.13	Biaxial	Theoretical	22

Fig. 8 Determination of Grüneisen parameters: (a) Schematic diagram of bending of graphene on PET substrate and (b) the corresponding Raman shift with increasing tensile strain. Reprinted with permission from ref. 8 Copyright (2022) from American Physical Society. (c) Illustration of MoS_2 bending measurement and its influence on Raman shift. Reprinted with permission from ref. 22 Copyright (2022) from IOP Publishing.

3. Applications of strain and doping model

While the evaluation of strain and doping is first used to understand the mechanisms in thermal annealing of graphene,[7,67] it could also be used for studying intrinsic mechanical and electronic properties of pristine 2D materials such as the contribution of strain and doping by structural defects,[14] the interaction of two layered materials in vertical heterostructure,[4,5,9,77] corrosion in 2D material covered metal surfaces[37] and textured surfaces,[11] and the temperature-dependent strain and doping measurements.[6,78,79] The above applications will be discussed individually in the following section.

3.1. Thermal annealing of graphene

While Lee et al.[67] demonstrated the modulation of compressive strain and hole doping due to thermal annealing of graphene on silica (Gr/SiO₂), the research continued to explore the origin of the phenomenon and its reversibility as shown in Fig. 9a.[7] The annealing of Gr/SiO₂ leads to compressive strain of 0.28%, which can be attributed to the lattice contraction. Given the negative thermal expansion coefficient (TEC) of graphene compared to the positive one of silica,[14,80] the expansion of graphene and the shrinking of underlying silica result in compressive strain of graphene during the cooling process.[81] Thermal annealing also reduces the electron concentration by 1×10^{13} cm^{-2} because of oxygen-mediated hole doping.[65] As for reversibility, water immersion counters the doping effect where the carrier concentration returns to the pristine undoped stage. Considering no further change in strain or doping after drying in ambient conditions,[7] it is shown that doping by thermal annealing is reversible by water immersion. The in situ measurement illustrates the edge of the graphene flake is quicker to achieve this water-induced recovery than the central region (i.e., basal plane),[7] suggesting the p-doping by annealing may be due to trapped oxygen beneath Gr/SiO₂[65] that the intercalation of water between Gr/SiO₂ interface leads to the replacement of oxygen molecules by water and thus the prohibition of oxygen-mediated hole doping. This speculation is supported by a separate measurement[7] where graphene is oxidised to form nanopores throughout the layer with subsequent annealing and immersion in water as shown in Fig. 9b. The shorter time required for the doping level to return to the pristine one, as well as the similar recovery speed between the edge and the inner region[7] suggests the nanopores provide additional intercalation channel to enable water diffusion to the Gr/SiO₂ interface.

Graphene annealing can be further studied by tuning the annealing temperature as well as re-annealing with the help of in situ Raman spectroscopy, as depicted in Fig. 9c.[18] Cooled Gr/SiO₂ after thermal annealing at 573 K shows a compressive strain of 0.13% and hole doping of 1.1×10^{13} cm^{-2}, agreeing well with previous experimental studies.[7,67] Higher annealing temperature at 973 K allows the compressive strain continues to develop but the doping level remains comparable. This result supports the earlier explanation that higher temperature culminates in a stronger lattice contraction effect while the oxygen-mediated p-doping has already taken place at low temperature and hence a higher temperature no longer strengthens the hole doping. It is also suggested that thermal annealing leads to closer contact between graphene layer and silica which increases the p-doping of graphene. While the air exposure of first-time annealed Gr/SiO₂ does not shift the Raman modes back to the pristine stage, real-time re-annealing studies[18] show that this Raman shifting is reversible starting from the second annealing cycle (compared to annealed graphene). This can be attributed to the carbon–carbon bond and phonon interactions that the irreversible changes (such as oxygen-mediated doping and changes in contact between graphene and substrate) are completed.

A comprehensive study of thermal annealing in graphene was carried out by Armano et al.[29] by heating Gr/SiO₂ under different gases, including vacuum, nitrogen, oxygen, and carbon dioxide with increasing number of time intervals as shown in Fig. 9d–g respectively. Pristine Gr/SiO₂ has an intrinsic compressive strain of 0.14% with negligible doping during the CVD fabrication. In vacuum and nitrogen environments, thermal treatment increases the compressive strain to 0.23% and 0.24% respectively but does not dope the sample. This effect is already observed in the first 20 minutes while longer treatment does not undergo any further modification. Thermal annealing under oxygen and carbon dioxide also leads to comparable compressive strain of 0.20% and 0.22%; however, significant p-doping occurs, reaching up to 1.22×10^{13} cm^{-2} and 0.6×10^{13} cm^{-2} respectively. It is worthy to note that with increasing heating time, oxygen mediated p-doping takes place in two steps: a fast and substantial hole doping ($0 \rightarrow 0.85 \times 10^{13}$ cm^{-2}, $0 \rightarrow 5$ min) followed by a slow and lesser hole doping (0.85×10^{13} cm$^{-2} \rightarrow 1.22 \times 10^{13}$ cm^{-2}, $5 \rightarrow 125$ min). These two processes may be either the adsorption of oxygen molecules to graphene at the basal plane,[82,83] or oxygen and water involved electron transfer in a redox reaction.[84,85] In contrast, the compressive strain is reduced back to the pristine stage with further temporal steps (>100 minutes), which may be associated with the softening in mechanical interaction by the intercalation of water molecules in Gr/SiO₂ interface.[29] As for the reversibility, the effect of air exposure is shown in Fig. 9h that graphene is de-doped from 1.28×10^{13} cm^{-2} to 0.78×10^{13} cm^{-2} after 465 hours in air. This de-doping process also occurs in two steps that the fading mainly takes place in the first 7 hours of air exposure. It is thus possible to interpret these results as two doping (and de-doping) stages. The fast and substantial doping and slow de-doping of 0.9×10^{13} cm^{-2} can be attributed to a low activation barrier and a deep energy trap which is probably due to the adsorption of oxygen molecules beneath graphene. Low activation barrier is due to minimal charge transfer in adsorption[86] while deep energy trap can be explained by the localisation of oxygen molecules on the Gr/SiO₂ interface protected from atmosphere by graphene, i.e., oxygen molecules between graphene and silica inducing p-doping cannot be reached
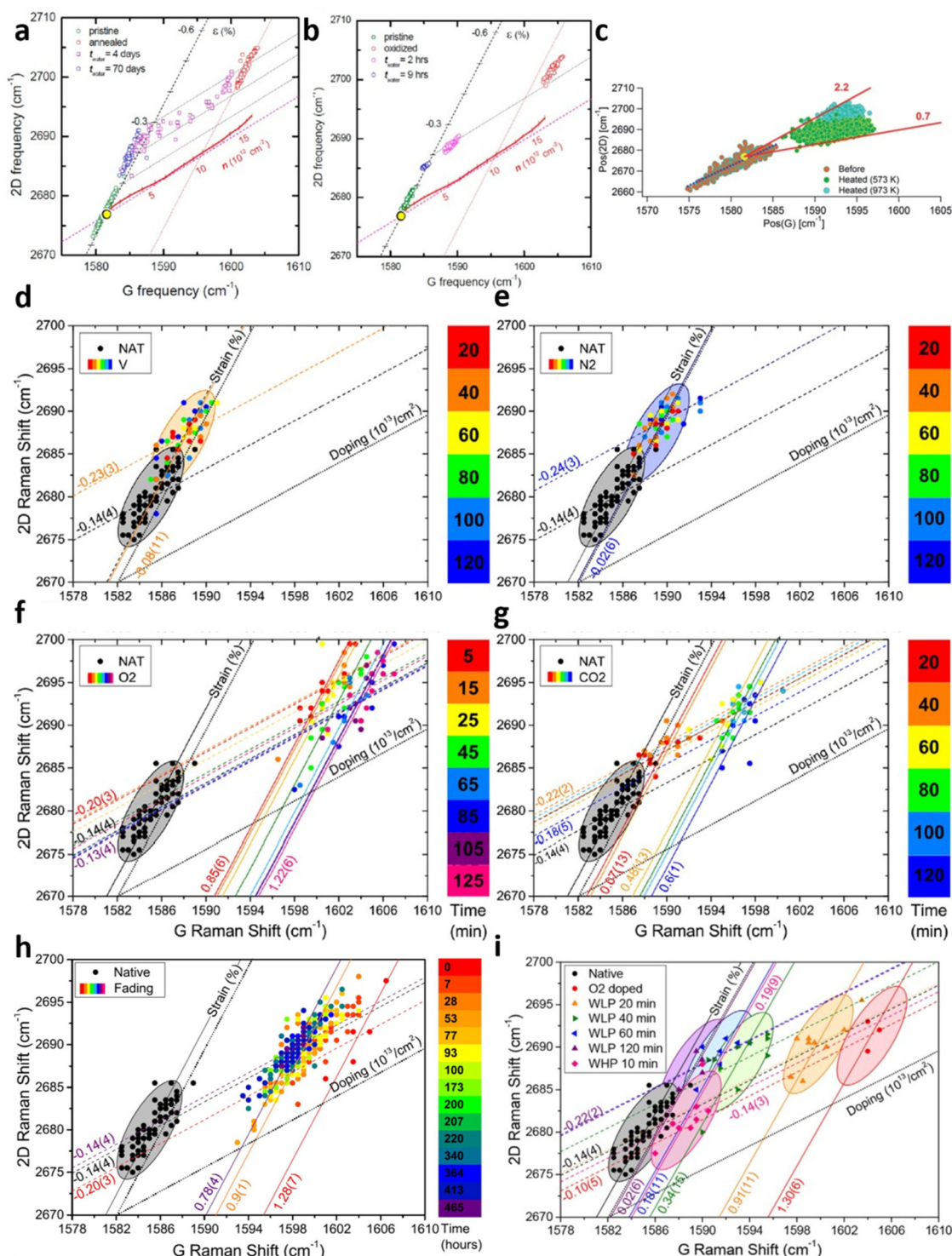
Fig. 9 Strain and doping evaluation in graphene annealing: (a) annealing effect and its water-induced recovery for pristine Gr/SiO$_2$ and (b) oxidised Gr/SiO$_2$. Reprinted with permission from ref. 7 Copyright (2022) from American Chemical Society. (c) Annealing effect at different elevated temperatures. Reprinted with permission from ref. 18 Copyright (2022) from RSC Publishing. (d) Annealing effect under vacuum, (e) nitrogen, (f) oxygen, and (g) carbon dioxide over time. NAT corresponds to native Gr/SiO$_2$. (h) De-doping effect of annealed graphene in air and (i) water over time. Reprinted with permission from ref. 29 Copyright (2022) from Elsevier.

easily by air.[69,82,83,87] The slow doping and fast de-doping of 0.4×10^{13} cm^{-2} can be correlated to high activation energy and shallow energy trap which is probably due to electron transfer

in redox reaction, as redox reaction needs a high energy barrier while large interaction of charges with atmosphere provides a low energy trap.[84,85] This theory can be further sup-

ported by *in situ* water immersion measurement in Fig. 9i. While the doping level of graphene is reduced by 0.4×10^{13} cm^{-2} in the first 20 min, corresponding to the second stage and is comparable to the air exposure environment, it continues to slowly drop to the pristine level associated to the first stage unlike air treatment, which is due to the ability of water diffusing across the graphene to remove the oxygen molecules on the Gr/SiO_2 interface.[7] With the help of strain and doping model, the mechanics of thermal annealing of graphene and its reversibility are extensively explored.

3.2. Modulation of strain and doping by structural defects and textured surfaces

With the benefit of the deconvolution model, the variation of strain and doping in pristine 2D materials culminated from structural defects in the manufacturing process were studied by Tripathi *et al.*[14] Combining the model with atomic force microscopy (AFM) enables the identification and measurement of common structural defects in different materials with different fabrication methods, including mechanically exfoliated (ME) graphene (Fig. 10a and b), chemical vapor deposited (CVD) graphene (Fig. 10c and d), ME MoS_2 (Fig. 10d and e), and CVD MoS_2 (Fig. 10f and g). In ME graphene, wrinkles are one of the common line defects arising from the balance between adhesion energy and bending energy during the transfer process.[88,89] Surprisingly, wrinkles with opposite influences to mechanical strain are recognised, which can be attributed to two different buckling orientations:[90,91] Small ripples with a height less than 8 nm tend to remain upright to form standing collapsed (SC) wrinkles as illustrated in the

inset of Fig. 10b, which correspond to a tensile strain (or release of compressive strain from surrounded basal plane) up to 0.5%. After exceeding this critical height, the excess bending energy leads to the bending of ripples towards the substrate which are referred as the transitional-folded (TF) wrinkles (Fig. 10b inset) and a compressive strain up to 0.5% is induced. The electronic modulations from these two types of wrinkles are also different. As compared to the defect-free region where Gr/SiO_2 is originally p-doped with a doping level of 4.2×10^{12} cm^{-2}, SC wrinkles reduce the p-doping to 2.6×10^{12} cm^{-2} and TF wrinkles exhibit a stronger inhibition against p-doping to 1.1×10^{12} cm^{-2}. This can be interpreted by the less coupling with the substrate in the buckled structure and the gap between graphene and silica is larger in TF than in SC wrinkles.[14,92] It is worth noting that the spatial resolution of the Raman probe can be estimated between 200 and 400 nm, depending on the laser wavelength and objective used.[14,93] While the resolution is usually larger than the defects, wrinkles, or sometimes the lateral size of the 2D materials, the influence of these effects can still be identified and resolved in the Raman signal. Due to small relative volumetric contribution, the scattering cross-section signals from the localised defects are weak, thus, individual point defects or vacancies in the nanoscale are challenging to be unambiguously characterised with Raman spectroscopy. Nonetheless, structural disorder such as wrinkles having smaller widths (10–40 nm) but larger lengths (few microns) can be well characterised by Raman spectroscopy. Several attempts have been taken to confine the laser into sub-diffraction limit and to enhance the scattering signals to the detectable level by gen-
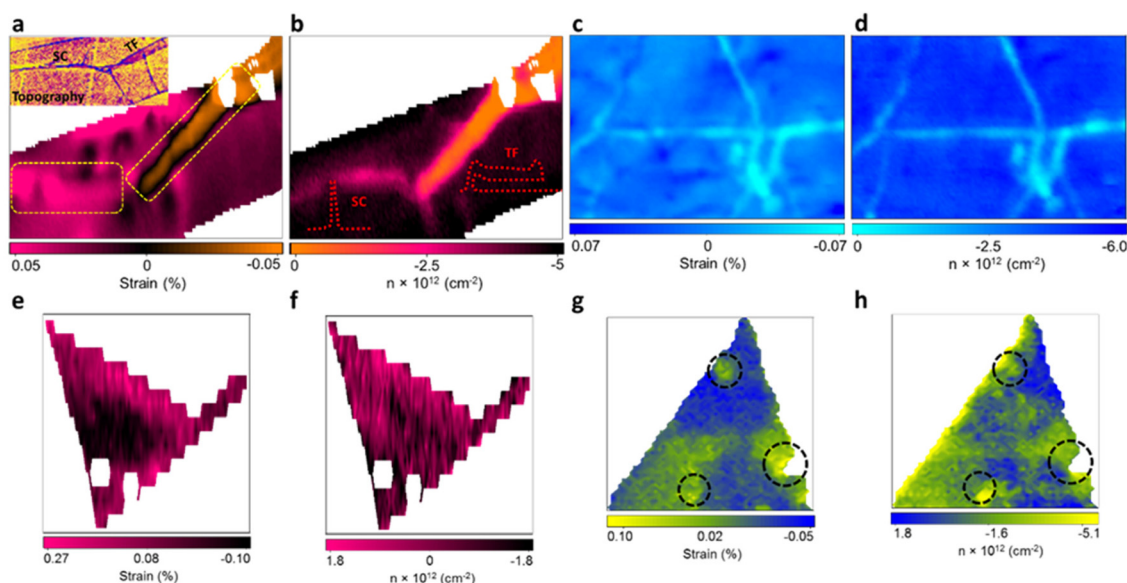

Fig. 10 Strain and doping maps of structural defects: (a) strain map of ME graphene showing standing collapsed (SC) (left dashed rectangle) and transitional folded (TF) wrinkles (right dashed rectangle). Inset shows the AFM image of topography for the identification of wrinkles. (b) The corresponding doping map of the same region in (a). Inset shows the schematic appearance of SC and TF wrinkles. (c) Strain and (d) doping map of CVD graphene showing the wrinkles in light blue colour. (e) Strain and (f) doping map of ME MoS_2 showing the inner defect free region (in black) and wrinkles near the edge (in pink). (g) Strain and (h) doping map of CVD MoS_2 showing the pit-holes as indicated by dashed circles. Reprinted with permission from ref. 14 Copyright (2022) from American Chemical Society.

erating a local plasmonics through localised light-metal interaction under surface-enhanced Raman spectroscopy (SERS) and tip-enhanced Raman spectroscopy (TERS) techniques.[94] Wrinkles are also observed in CVD graphene (Fig. 10c and d) due to its lower TEC than that of substrate and thus the lattice mismatch during the cooling process in fabrication.[80] A compressive strain up to 0.051% and a reduction of p-doping of 2.18×10^{12} cm^{-2} are measured in the wrinkles region, which is comparable to the TF wrinkles in ME graphene.

In ME MoS$_2$ (Fig. 10e and f), while the defect-free centre region displays accumulation of compression strain ranging from 0.01% to 0.09%, the wrinkles near the edge release the intrinsic compressive strain into a tensile strain of 0.14 to 0.27%. An increase in electron concentration is also observed at the wrinkles region, suggesting the tensile strain in wrinkles be responsible for the increase in the mobility of the charge carrier.[14,95] In CVD MoS$_2$ (Fig. 10g and h), the defect-free region possesses a higher built-in tensile strain than ME system, which is due to the TEC mismatch between MoS$_2$ and silica substrate.[96] This tension on the basal plane also prevents the formation of wrinkles. Pit-holes, another structural defect, however, emerge from the etching of the silica substrate by alkali metal precursors in CVD fabrication[97] and culminates in tensile strain varying from 0.01% to 0.07% with a wide range of modulation on doping. This can be attributed to the bending along the circular trench in pit-hole regions.[14] The above results of doping in structural defects are in good agreement with separate Kelvin probe force microscopy (KPFM) measurements, suggesting the versatility for the strain and doping model. While the structural defects modulate the strain distribution, they are randomly spread over the surface

which is difficult to regulate. Therefore, controlled strained and doped systems can be achieved through deposition of 2D material over periodic arrays or on textured surfaces, where the protruded surface induces local stretching and contraction of the flexible 2D material. The extent of strain depends on the aspect ratio (height or width/spacing between the protruded regions) of the textured surface and interfacial interactions.[98] Recently, a systematic Si grooved surface of different pitch lengths (40 nm, 125 nm and 250 nm) at comparable depth has been investigated (Fig. 11a–c).[11] The conformation of the graphene layer to each patterned surface induces different strain between crest and trough regions, which can be validated by Raman mapping through the deconvolution model (Fig. 11d). It has been observed that the flat Si surface induces compressive strain in the graphene which systematically decreases over textured surfaces with reducing pitch length. Such textured architectures were useful to study nanoscale cog of nanogears for the lubrication nanoscale devices. A similar work is presented by the deposition of graphene over silica nanospheres of different diameters, in which the optimised strain distribution around the spherical shaped was used to explore strain engineering in graphene.[98]

The optomechanical measurement using MoS$_2$ has been carried out over Si/silica nanopillar arrays (height 420 nm and 820 nm) as shown in Fig. 11e.[25] The strain in the suspended MoS$_2$ is regulated by introducing a "tent" structure around the nanopillars. Raman measurements indicate the appearance of the highest strain at the centre of the pillar's apex (Fig. 11f). By monitoring the shift in E$^1_{2g}$ and A$_{1g}$, a tensile strain of around 2% has been evaluated, which was claimed to be undervalued due to laser spot size restriction. The maximum
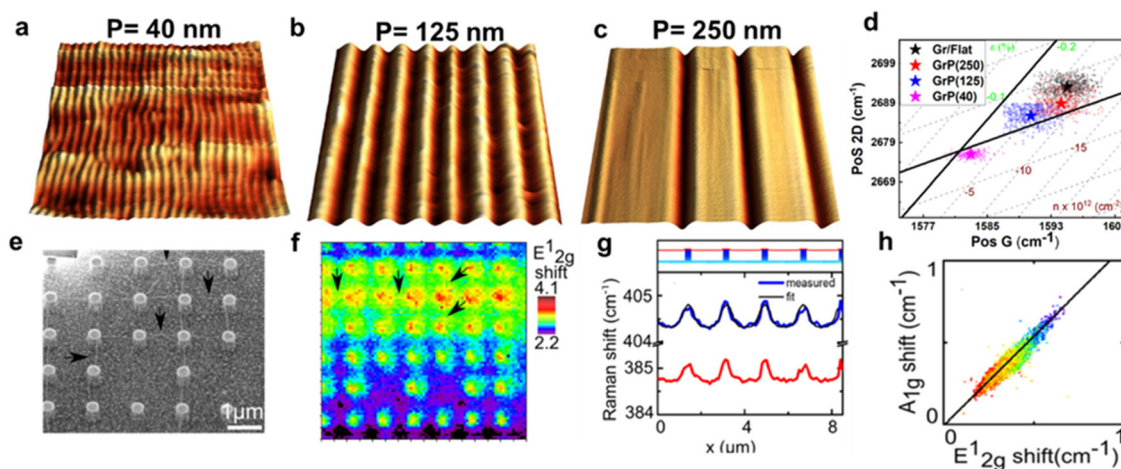

Fig. 11 Textured induced strain and doping in 2D materials: (a–c) 3D AFM images of graphene-covered Si textured surface of different pitch lengths: 40, 125, and 250 nm, respectively. (d) Correlation plot of graphene over different textured surfaces showing trend of strain and doping with various extent of conformation. Reprinted with permission from ref. 11 Copyright (2022) from John Wiley and Sons. (e) SEM (scanning electron microscopy) micrograph of MoS$_2$-covered pillar-shaped structure. (f) Raman map showing the shift in E$^1_{2g}$ peak position over the pillar as compared to the flat surface. The marked arrows represent the Raman signal from ripples generated due to strain between two or more nanopillars. (g) Line profile from Raman spectroscopy showing distinguishable shift in Raman modes (E$^1_{2g}$ and A$_{1g}$) of MoS$_2$ between pillars and basal surface. (h) Correlation plot showing a trend in the Raman modes, and the solid line revealing the linear trend. Reprinted with permission from ref. 25 Copyright (2022) from American Chemical Society.

strain was anticipated up to 2.4%. The contribution of doping has been determined by measuring the Raman line profile for peak shift in E^1_{2g} and A_{1g}. The results reveal that the modulation in A_{1g} is more effective than E^1_{2g} (up to 8.2 times) that depicts a strong doping-dependent signature (Fig. 11g). The correlation plot revealed a linear dependence with a slope of 1.1 indicating the influence of the electron–phonon interaction (Fig. 11h).[25]

3.3. Strain and doping in vertical heterostructure

Vertical heterostructures of 2D materials have been used to exploit the synergy from individual layers for a range of applications. Graphene over hexagonal boron nitride (hBN) and MoS_2 are among the common examples of vertical heterostructures. Given that hybrid architecture of Gr/hBN is related to field-effect tunnelling[99] and Anderson localisation which results in metal–insulator transition,[100,101] an investigation of the effect of beneath hBN to the top layer graphene is thus illustrated in Fig. 12a.[9] By comparing Gr/hBN with Gr/SiO_2 under ambient conditions, the doping from hBN to graphene is found to be insignificant, while hBN induces additional 0.1% compressive strain to graphene compared to Gr/SiO_2. The thermal annealing at 673 K barely induces hole doping in Gr/hBN (3×10^{12} cm^{-2}) which is less than that of Gr/SiO_2 (1×10^{13} cm^{-2}), possibly due to hydrophobic hBN attracting fewer water molecules in the interface for doping[65,102,103] or the reduction in ripple formation in highly flat hBN.[65,67,104]

The model can also be applied for the examination on an innovative graphene spin-valve device comprising of MgO/Co, SiO_2, and hBN/Gr as depicted in Fig. 12b.[24] In the device, hBN/Gr is partly suspended and partly supported on SiO_2, and the strain and doping evaluation indicates slight doping ($<5 \times 10^{11}$ cm^{-2}) in the suspended region but significant doping (3×10^{12} cm^{-2}) in SiO_2 supported region. The substantial doping may be due to vacancies or charged defects in MgO/Co electrodes as well as local electric field in SiO_2.[105,106] On the other hand, insignificant strain is observed in suspended region while compressive strain of 0.2% is measured at SiO_2 supported region, which may arise from the bending of graphene or substrate-induced effect.[67,107]

Another inspection of strain and doping distribution was performed in hBN/Gr/SiO_2 and hBN/Gr/hBN heterostructures as shown in Fig. 12c and d respectively.[31] In the former hybrid, hBN induces compressive strain to graphene owing to the difference in TEC,[108] leading to a transition of 0.5% tensile strain in bare graphene to 0.1% compressive strain in hBN-covered graphene region. hBN also results in a decrease in p-doping from 3×10^{12} cm^{-2} to 1×10^{12} cm^{-2} by shielding graphene from any environmental adsorbates.[31] When graphene is sandwiched between two hBN flakes (Fig. 12d), the strain and doping distribution is less spread, implying the encapsulation provides an insulation from external factors causing the variation. The overall compressive strain of flat graphene is between 0.03% and 0.06%; however, in large bubbles, a tensile strain of 0.06% is induced. There are also small bubbles releasing the compressive strain of graphene to almost non-strained

condition. The overall graphene is charge-neutral because of the hBN protection from adsorbates and the prohibition of doping from SiO_2 substrate. Bubble regions, however, show a slight p-doping up to 0.6×10^{12} cm^{-2}, which may be attributed to changes in Gr/hBN interaction near the cavity edge owing to interlayer separation or hBN edge potentials.[109,110]

Given that Gr/MoS_2 heterostructure is of interest for applications including optoelectronics and photovoltaics,[111–113] the deconvolution model allows the evaluation of induced strain and doping of both materials, which is extensively studied in Fig. 12e–g.[35] While bare graphene is originally p-doped with doping level of 1.4×10^{13} cm^{-2} and experiences tension up to 0.3%, the embedding by MoS_2 causes a reduction of p-doping to 0.4×10^{13} cm^{-2} and a transition from tensile to compressive strain up to 0.3% (Fig. 12f). The measurement on MoS_2 Raman modes (Fig. 12g) reveals that MoS_2 conversely becomes p-doped and undergoes a drop in tension (compression) in the presence of graphene. Both results demonstrate a donation of electrons from MoS_2 to graphene which can be explained by electron-rich feature of MoS_2 compared to electron-poor graphene. The induced strain can also be interpreted by different TEC between graphene and MoS_2 which leads to lattice mismatch during the CVD process.[4,62,114] To examine the possibility of modulation in strain or carrier concentration, both samples are annealed at 623 K in argon.[35] Graphene is further p-doped and compressed after annealing, as expected due to the oxygen residue trapped in the interface and the lattice contraction.[67,115] While this culminates in an absolute shift in strain and doping of both Gr and Gr/MoS_2, the difference in strain and doping among them remains comparable, i.e., the thermal annealing does not alter the relative strain and doping in graphene due to the embedding of MoS_2. This is also supported by a similar response in MoS_2 annealing in argon[35] that the strain and doping modulation are absolute but not relative.

3.4. Graphene on metal surfaces

Hybrid between graphene and silver nanowire (AgNW) has recently attracted considerable interest in light of the conductivity enhancement in transparent electrodes as well as the improved performance of photovoltaic devices due to surface plasmon resonance.[5,110,116] It is thus rational to study the induced strain and doping in the vertically stacked heterostructure in either Gr/AgNW (Fig. 13a and b) and AgNW/Gr (Fig. 13c) orientation.[5] In the former system, the underneath AgNW does not lead to discernible doping but induces tensile strain up to 0.06% to the upper graphene layer, indicating the conformation of graphene by the AgNW. In latter (Fig. 13c), the topping of AgNW on graphene exhibits a similar response, albeit weaker, of negligible doping and 0.01% tensile strain. This can be inferred by a slight extension of carbon–carbon bonds as compared to Gr/ITO.[5]

Given copper being the most widely employed substrate for CVD graphene fabrication,[117] a detailed understanding of the interplay between the copper catalyst and graphene will thus be essential. The strain and doping evaluation serve as a
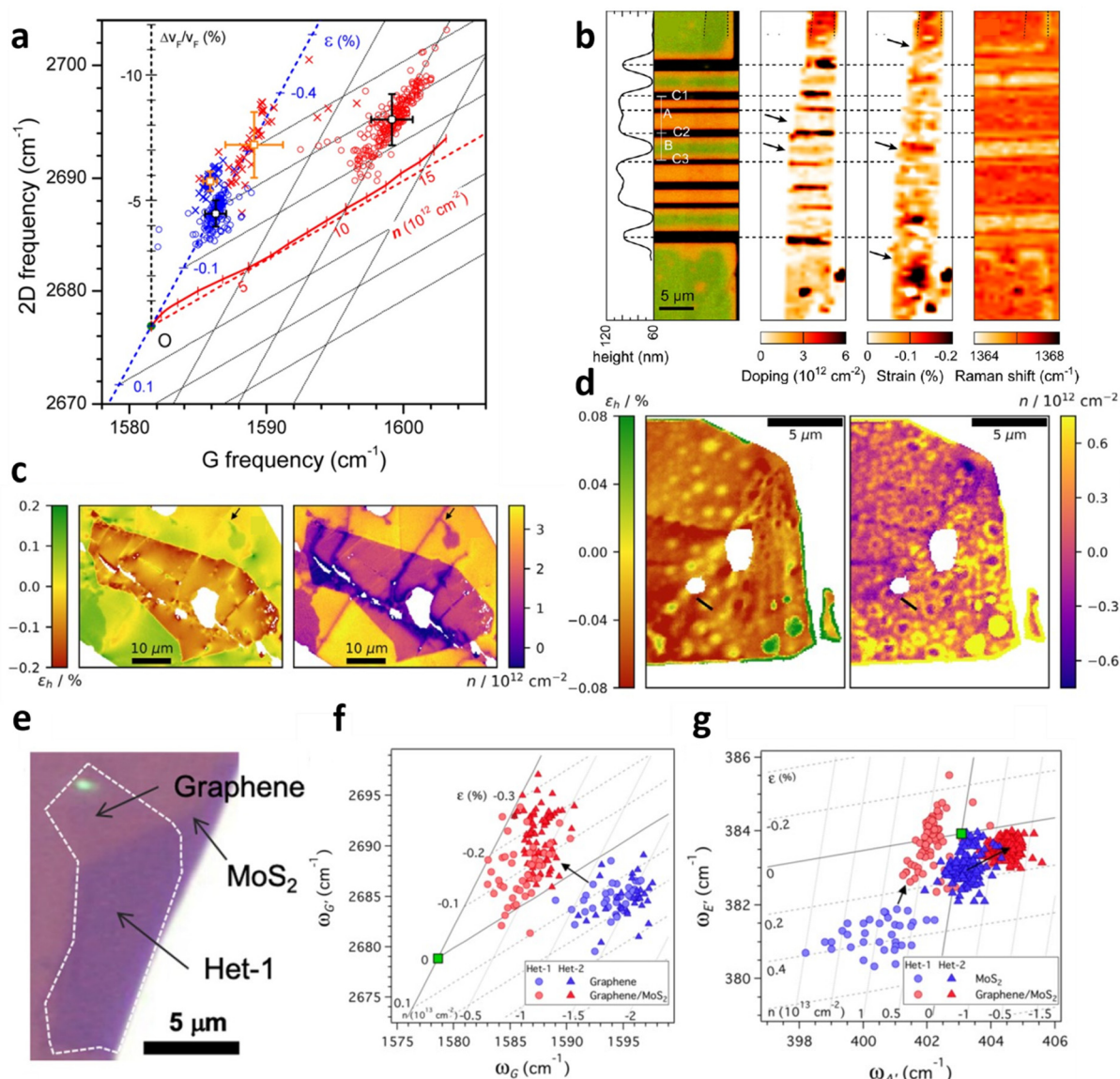
Fig. 12 Interaction between graphene and hBN: (a) correlation plot of the hBN and annealing effect to graphene. Circles represents bare graphene and crosses represents Gr/hBN. Blue colour corresponds to before annealing and red colour corresponds to after annealing for 2 h at 673 K. Reprinted with permission from ref. 9 Copyright (2022) from American Chemical Society. (b) Left to right: false colour image for hBN/Gr on different substrate, doping map, strain map, and Raman shift. In false colour image, black represents hBN/Gr on MgO/Co electrode, green represents hBN/Gr on silica substrate, and orange corresponds to suspended hBN/Gr. Reprinted with permission from ref. 24 Copyright (2022) from American Chemical Society. (c) Strain and doping map of hBN/Gr/SiO$_2$. hBN locates at the middle of the image while Gr/SiO$_2$ substrate constitutes the background. (d) Strain and doping map of hBN/Gr/hBN. Reprinted with permission from ref. 31 Copyright (2022) from IOP Publishing. (e) Optical image of graphene over MoS$_2$. (f) Correlation plot of Gr/MoS$_2$ in the perspective of graphene and (g) MoS$_2$. Circles and triangles correspond to different samples. Reprinted with permission from ref. 35 Copyright (2022) from American Physical Society.

powered tool to investigate the effect of crystalline nature and the lattice orientation of copper on the graphene growth, which is illustrated in Fig. 14a.[4] The magnitude of compressive strain induced on graphene is highly dependent on the lattice orientation of copper as the following order: Cu (111) > Cu (110) > Cu (100). The vector analysis reveals that Cu (111) induces an additional 0.2% compressive strain when compared to Cu (100), which may be due to the different mismatch between lattice parameter of copper and equilibrium C–C

bond length during the formation of different superstructure of graphene at Cu (111) and Cu (100).[4,118] This result agrees with a separate molecular dynamics simulation[118] suggesting a higher compressive strain in Cu (111) than Cu (100).

Formation of graphene wrinkles on metal surface also provides a magnificent example for the deconvolution model. As shown in Fig. 14b and c,[19] the strain and doping distribution of Gr/Co wrinkles are studied. While minimal doping (a change of carrier concentration less than 1.3×10^{12} cm^{-2})
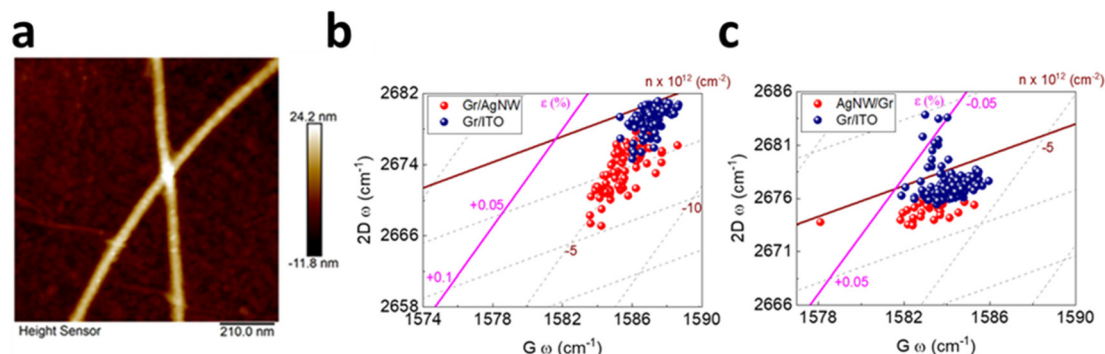
Fig. 13 (a) AFM image of graphene covered AgNW. (b) Correlation plot of Gr/AgNW and (c) AgNW/Gr heterostructure. Blue colour represents bare graphene while red colour represents incorporation of AgNW. Reprinted with permission from ref. 5 Copyright (2022) from MDPI.
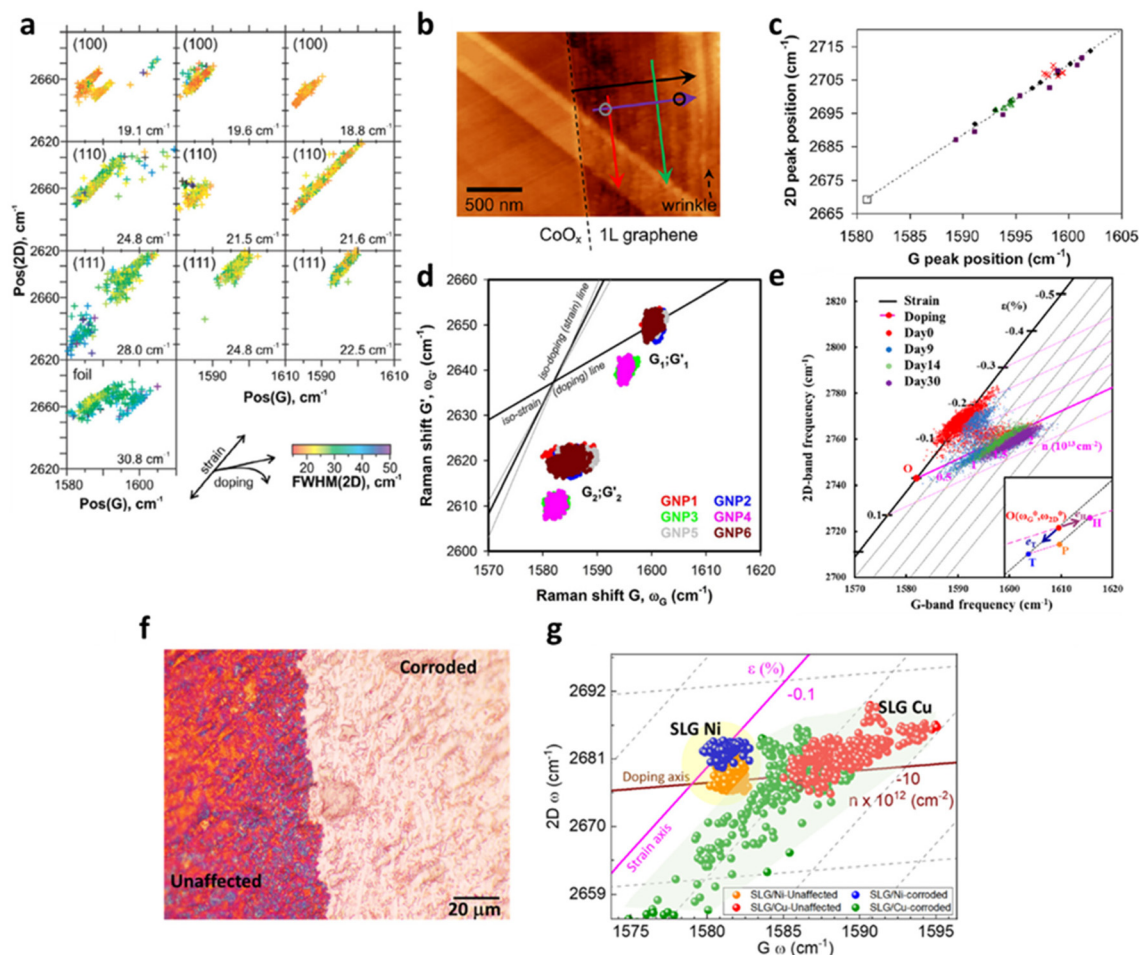

Fig. 14 Correlation plots of graphene on metal surfaces: (a) correlation plot of graphene on Cu with different lattice orientations including Cu (100), Cu (110) and Cu (111). Reprinted with permission from ref. 4 Copyright (2022) from Elsevier. (b) AFM image and (c) the correlation plot of graphene on Co. The colour of the arrows in the AFM image represents the data points in the correlation plot. Graphene near the edge (red) shows a larger compressive strain than graphene in the inner area (green). Reprinted with permission from ref. 19 Copyright (2022) from American Chemical Society. (d) Correlation plot of graphene on NPs. G_1; G'_1 corresponds to the flat region and G_2; G'_2 corresponds to wrinkled region. Reprinted with permission from ref. 30 Copyright (2022) from Springer Nature. (e) Correlation plot of graphene on Cu with time. Reprinted with permission from ref. 34 Copyright (2022) from American Chemical Society. (f) Optical image of graphene over Cu surface which is partially exposed to a strong acid (H_2SO_4), where both regions have been taken for the Raman analysis. (g) Correlation plot of graphene single layer (SLG) over Cu and Ni showing tension in the corroded region as compared to unaffected. Reprinted with permission from ref. 37 Copyright (2022) from American Chemical Society.

takes place across the entire graphene sheet, compressive strain of 0.38% is induced at the supported region in Gr/Co, which can be attributed to the TEC difference that graphene expands when it is cooled during the fabrication process. A larger compressive strain is induced near the edge than the central region, and hence it can be speculated that the edge of graphene is pinned with the strongest compressive strain, which is gradually relieved along the inner region until wrinkles are generated where compressive strain is the lowest.[119–122] A separate measurement[19] indicates that compressive strain recovers in between wrinkles, leading to an intriguing phenomenon of 'strain field'. A deliberate wrinkle generation can also be performed by depositing graphene on iron oxide nanoparticles (NPs) on SiO_2 where the induced strain and doping are studied in Fig. 14d.[30] Wrinkles are formed by the curvature of NPs and successfully located as G_2; G'_2 from the flat region (G_1; G'_1) corroborated from AFM results. In low wrinkling area, graphene is heavily p-doped (1.3×10^{13} cm^{-2}) with insignificant strain which is due to large area coupling with the SiO_2 substrate, while high wrinkling reduces the hole doping to 1.2×10^{13} cm^{-2} with 0.06% tensile strain due to less contact area with the substrate.[30,123]

The modulation of strain and doping in graphene by the morphology of metal substrate can also be realised by growing graphene on Cu where Cu gradually oxidises to form Cu_2O as illustrated in Fig. 14e.[34] Recent studies[124–126] show that the attachment of water molecules to the structural defects of graphene such as wrinkles and grain boundaries leads to the oxidation of Cu to Cu_2O. Between day 0 and day 9, graphene remains compressive (0.15%) with no doping ($<1 \times 10^{12}$ cm^{-2}). With increasing oxidation of Cu beneath, the compressive strain is completely released to non-strained condition and becomes p-doped. On day 30 and onwards, tensile strain even develops in graphene and p-doping increases to 1×10^{13} cm^{-2}. In situ measurement demonstrates this strain and doping effect is faster on defect sites such as wrinkles. The overall result can be explained as graphene initially possesses compressive strain due to lower TEC of graphene than Cu,[4,19] the curvature by the oxidation of Cu into Cu_2O particles releases the compressive strain.[34] As Cu_2O is a p-type semiconductor with a band gap of 2.17 eV,[127] graphene is also gradually p-doped with time. As the defect sites provide more diffusion pathway for oxidation, accelerated tension generation and hole doping response at that area are recognised.

In addition to the nanoscopic investigation of graphene wrinkles, the chemical and physical changes in Cu foil by corrodents (H_2SO_4) are successfully identified by graphene through strain and doping at the micro scale.[37] Partial surface of polycrystalline Cu exposed to the H_2SO_4 are physically etched the Gr/Cu surface (Fig. 14f) and affects the carrier concentration (Fig. 14g). By observing a similar phenomenon over graphene deposited on Ni surface, it is suggested that the presence of grain boundaries permeates the corrodents and etches the metal surfaces, causing tension in the graphene layer. Considering the grain boundaries as the weak centre of single layer graphene, multi-layered system has been implemented to

protect the Cu surface from biotic and abiotic corrosion, which shows promising results. Thus, the topping of graphene layer can act as a corrosion sensing medium.

3.5. Temperature-dependent strain and doping

In situ Raman measurement at different temperatures can reveal crucial information of graphene and MoS_2 such as TEC,[78,80,128] thermal conductivity,[129,130] and the strain and doping modulation by external heat.[6,79] At elevated temperatures, strain and doping are no longer the exclusive factors for the shift of Raman modes; instead, the lattice expansion and anharmonic coupling also lead to the phonon shifts.[130–132] The addition of these thermal influences to eqn (9) results in

$$\Delta\omega_i = 2\gamma_i\omega_i^0\varepsilon + k_i n + \Delta\omega_i^{LE} + \Delta\omega_i^A \quad (13)$$

where $\Delta\omega_i^{LE}$ and $\Delta\omega_i^A$ represent the lattice expansion and anharmonicity effect. The Δ sign means the change of the absolute thermal effect, $\omega_i^{LE}(T)$ and $\omega_i^A(T)$, at the elevated temperature T_E from the reference temperature T_R, i.e., $\Delta\omega_i^{LE} + \Delta\omega_i^A = \omega_i^{LE}(T_E) + \omega_i^A(T_E) - (\omega_i^{LE}(T_R) + \omega_i^A(T_R))$. For graphene, this combined thermal effect $\omega_i^{LE}(T) + \omega_i^A(T)$ has been extensively studied and the value can be approximated by a third-order polynomial.[131,133] For MoS_2, this term is reported to be linearly proportional to temperature and can be estimated by a first order polynomial.[129,130] The general accepted values[129,131,133] are therefore listed in eqn (14) and Table 3.

$$\omega_i^{LE}(T) + \omega_i^A(T) = c_0 + c_1 T + c_2 T^2 + c_3 T^3 \quad (14)$$

After subtracting the thermal influences in eqn (13), the strain and doping become the only factors altering the phonon shifts. The assumption of temperature invariance of Grüneisen parameter and doping coefficient allows the re-implement of the strain and doping model. A typical example of this application will be the TEC evaluation of 2D materials,[78,80,128] which involves the deposition of the 2D materials on TEC known substrate (usually SiO_2) with subsequent heating. The strain developed from the TEC mismatch can then be monitored by Raman spectroscopy and the TEC of the 2D material can hence be calculated:

$$\begin{aligned}\varepsilon &= \int_{T_R}^{T_E} \alpha_{SiO_2}(T) - \alpha_{2D\,material}(T)\mathrm{d}T \\ &= \frac{\Delta\omega_i - (\Delta\omega_i^{LE}(T) + \Delta\omega_i^A(T))}{-2\gamma_i\omega_i^0}\end{aligned} \quad (15)$$

where α represents the TEC. The realisation of the temperature-dependent strain and doping model was also attempted

Table 3 Constants for lattice expansion and anharmonic coupling

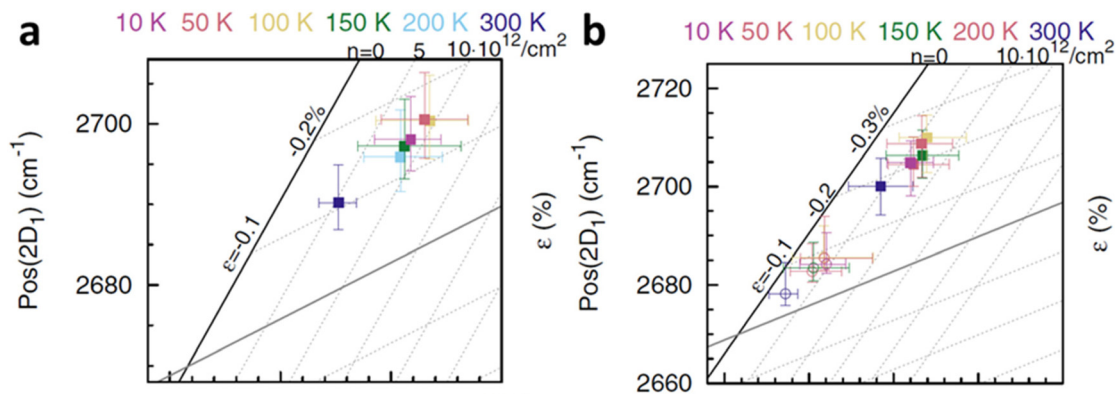| i	c_0 (cm^{-1})	c_1 (cm^{-1} K^{-1})	c_2 (cm^{-1} K^{-2})	c_3 (cm^{-1} K^{-3})
E^1_{2g}	4.101	-13.9×10^{-3}	0	0
A_{1g}	3.835	-13×10^{-3}	0	0
G	2.466	-4.23×10^{-4}	-3.03×10^{-5}	1.15×10^{-8}
2D	2.442	-3.70×10^{-3}	-5.10×10^{-6}	-3.53×10^{-8}

Fig. 15 Temperature-dependent strain and doping of (a) monolayer graphene and (b) isotopically labelled bilayer graphene. Open circles represent the top layer while filled squares represent the bottom layer. Reprinted with permission from ref. 6 Copyright (2022) from American Physical Society.

by Verhagen *et al.*[6] to study the cooling effect on monolayer and bilayer isotopically labelled graphene as shown in Fig. 15a and b respectively. The monolayer graphene is susceptible to the generation of compressive strain when the temperature is reduced from ambient to 100 K; the compression is then saturated at 50 K and even decreases back at 10 K. This compression can be attributed to the TEC mismatch between graphene and SiO_2 substrate.[80] On the other hand, p-doping occurs significantly when the temperature decreases from ambient to 200 K, and the successive cooling does not produce any profound effect. In bilayer, the top layer and bottom layer graphene respond similarly in strain that compression is generated when they are first cooled, which is reduced during further cooling. The doping response between the two layers is different: the p-doping level of the top layer remains almost constant until 10 K and starts to increase after 50 K, while the bottom layer is p-doped when the temperature decreases from ambient to 200 K and the doping level fluctuates beyond that. The temperature induced strain and doping are always stronger in the bottom graphene layer as compared to the top layer, which is due to indirect contact with SiO_2 substrate that the additional graphene layer provides lubricating (weak vdW interface) and charge screening effect.[6]

4. Conclusions

In this review, the fundamentals of strain and doping in 2D materials including graphene and MoS_2 are addressed. Under mechanical strain, the change of lattice arrangement leads to a shift in electronic band structure of layered materials, which can be illustrated by the symmetries in hexagonal Brillouin zone for graphene and is related to the transition of direct to indirect band gap for MoS_2. Under electrical doping, the relations between applied top gated voltage, surface charge density, and electrical conductivity are extensively demonstrated in different materials. The principles of chemical doping on zero band gap graphene and other semiconductors

are also addressed. The combination of strain and doping leads to a shift of Raman modes, which is found to be linearly independent and can be deconvoluted with the help of a correlation plot of Raman peak positions of G and 2D for graphene, and E^1_{2g} and A_{1g} for MoS_2. Several empirical and theoretical methods for the computation of the weightings in such linear transformation, *i.e.*, Grüneisen parameters and doping coefficients, are also presented.

This deconvolution method allows for a non-invasive evaluation of strain and doping of 2D materials on a nanoscopic scale, with higher resolution than conventional techniques such as piezoresistive approaches and field-effect measurements. The simultaneous evaluation of mechanical strain and electrical doping also provides more comprehensive insight than scanning probe techniques such as KPFM, which can only unveil the electrical information.[134] The model therefore enables the investigation of a variety of aspects including intrinsic studies, interactions in hybrid vertical heterostructure, corrosion protection, and temperature-dependent studies. An in-depth understanding of the graphene annealing process and its corresponding de-doping results are discussed with the help of correlation plot, where the thermal annealing process can be divided into two steps—a fast doping stage attributed to adsorption of oxygen molecules beneath graphene, and a slow doping stage due to electron transfer in redox reaction. The intrinsic studies of pristine CVD and ME 2D materials show a transition of tensile strain to compressive strain in graphene wrinkles depending on the wrinkles configuration (standing collapsed orientation or transitional-folded). A reduction in p-doping is also observed for graphene wrinkles due to less coupling with the substrate. Recent studies also suggest the generation of patterned compressive strain by depositing 2D materials on a textured surface such that the local strain can be engineered for flexible devices.

The strain and doping studies of hybrid vertical heterostructure become possible thanks to the deconvolution method. The extensive investigation on the interplay between graphene and hBN layers shows that hBN provides protection

and charge screening to graphene. Similar inspections are carried out for Gr/MoS$_2$ and Gr/AgNW heterostructure where different contributions to mechanical strain and charge transfer are unveiled by the correlation plot. The release of compressive strain in graphene by the oxide formation and the change in carrier concentration in graphene by the acid corrosion in Gr/Cu demonstrates the feasibility of graphene serving as a chemical sensor. Temperature dependent strain and doping deconvolution allow the computation of TEC and the analysis of the modulation on materials behaviour in low temperature environment. The above applications demonstrate that the strain and doping deconvolution provide an intriguing insight into the emerging field of straintronics where graphene and other 2D materials can be engineered into innovative flexible electronics. The Raman based diagnostic readout is also capable of onsite detection of chemical oxidation and corrosion. Moreover, most biological species which are not Raman active can be exclusively detected from the perspective of 2D materials in terms of strain and doping which is relatively fast and non-invasive than other conventional techniques. Future directions include constructing the strain and doping model to other 2D materials whose Raman active modes are sensitive to mechanical deformation and electronic doping. The determination of the Grüneisen parameters and doping rate of the material could enable the linear transformation of the deconvolution. However, the requirement of possessing two Raman modes which are both independently sensitive to strain and doping limits the employment of this model to many other 2D materials. To date, only graphene and MoS$_2$ are reported to fulfil this prerequisite.[22,35,69] It is also possible to apply the model to a variety of research fields such as medical screening, gas sensing and flexible optoelectronics by observing the modulation of strain or doping by foreign molecules, corrosion or oxidation.

Author contributions

FL and MT wrote the manuscript with assistance from RSS, SPO, AAG, IJ and ABD.

Conflicts of interest

There are no conflicts to declare.

Acknowledgements

References

1 A. Molina-Sanchez and L. Wirtz, *Phys. Rev. B: Condens. Matter Mater. Phys.*, 2011, **84**, 155413.

2 J. H. Chen, C. Jang, S. Adam, M. S. Fuhrer, E. D. Williams and M. Ishigami, *Nat. Phys.*, 2008, **4**, 377–381.

3 H. Pinto and A. Markevich, *Beilstein J. Nanotechnol.*, 2014, **5**, 1842–1848.

4 O. Frank, J. Vejpravova, V. Holy, L. Kavan and M. Kalbac, *Carbon*, 2014, **68**, 440–451.

5 F. Lee, M. Tripathi, P. Lynch and A. B. Dalton, *Appl. Sci.*, 2020, **10**, 5157.

6 T. G. A. Verhagen, K. Drogowska, M. Kalbac and J. Vejpravova, *Phys. Rev. B: Condens. Matter Mater. Phys.*, 2015, **92**, 125437.

7 L. Yu, Y.-H. Lee, X. Ling, E. J. G. Santos, Y. C. Shin, Y. Lin, M. Dubey, E. Kaxiras, J. Kong and H. Wang, *Nano Lett.*, 2014, **14**, 3055–3063.

8 T. M. G. Mohiuddin, A. Lombardo, R. R. Nair, A. Bonetti, G. Savini, R. Jalil, N. Bonini, D. M. Basko, C. Galiotis and N. Marzari, *Phys. Rev. B: Condens. Matter Mater. Phys.*, 2009, **79**, 205433.

9 G. Ahn, H. R. Kim, T. Y. Ko, K. Choi, K. Watanabe, T. Taniguchi, B. H. Hong and S. Ryu, *ACS Nano*, 2013, **7**, 1533–1541.

10 A. Das, S. Pisana, B. Chakraborty, S. Piscanec, S. K. Saha, U. V. Waghmare, K. S. Novoselov, H. R. Krishnamurthy, A. K. Geim and A. C. Ferrari, *Nat. Nanotechnol.*, 2008, **3**, 210–215.

11 A. Mescola, G. Paolicelli, S. P. Ogilvie, R. Guarino, J. G. McHugh, A. Rota, E. Iacob, E. Gnecco, S. Valeri and N. M. Pugno, *Small*, 2021, **17**, 2104487.

12 E. Y. Andrei, G. Li and X. Du, *Rep. Prog. Phys.*, 2012, **75**, 056501.

13 B. G. Shin, G. H. Han, S. J. Yun, H. M. Oh, J. J. Bae, Y. J. Song, C. Y. Park and Y. H. Lee, *Adv. Mater.*, 2016, **28**, 9378–9384.

14 M. Tripathi, F. Lee, A. Michail, D. Anestopoulos, J. G. McHugh, S. P. Ogilvie, M. J. Large, A. A. Graf, P. J. Lynch and J. Parthenios, *ACS Nano*, 2021, **15**, 2520–2531.

15 C. Lee, H. Yan, L. E. Brus, T. F. Heinz, J. Hone and S. Ryu, *ACS Nano*, 2010, **4**, 2695–2700.

16 K. S. Novoselov, A. K. Geim, S. V. Morozov, D. Jiang, M. I. Katsnelson, I. Grigorieva, S. Dubonos and A. Firsov, *Nature*, 2005, **438**, 197–200.

17 X. Zhang, Z. Shao, X. Zhang, Y. He and J. Jie, *Adv. Mater.*, 2016, **28**, 10409–10442.

18 S. D. Costa, J. E. Weis, O. Frank, M. Fridrichová and M. Kalbac, *RSC Adv.*, 2016, **6**, 72859–72864.

19 M. S. Bronsgeest, N. Bendiab, S. Mathur, A. Kimouche, H. T. Johnson, J. Coraux and P. Pochet, *Nano Lett.*, 2015, **15**, 5098–5104.

20 G. Cocco, E. Cadelano and L. Colombo, *Phys. Rev. B: Condens. Matter Mater. Phys.*, 2010, **81**, 241412.

21 J. Yan, Y. Zhang, P. Kim and A. Pinczuk, *Phys. Rev. Lett.*, 2007, **98**, 166802.

22 A. Michail, D. Anestopoulos, N. Delikoukos, J. Parthenios, S. Grammatikopoulos, S. A. Tsirkas, N. N. Lathiotakis, O. Frank, K. Filintoglou and K. Papagelis, *2D Mater.*, 2020, **8**, 015023.

23 D. Rhodes, S. H. Chae, R. Ribeiro-Palau and J. Hone, *Nat. Mater.*, 2019, **18**, 541–549.

24 M. Drögeler, F. Volmer, M. Wolter, B. Terrés, K. Watanabe, T. Taniguchi, G. Güntherodt, C. Stampfer and B. Beschoten, *Nano Lett.*, 2014, **14**, 6050–6055.

25 J. Chaste, A. Missaoui, S. Huang, H. Henck, Z. Ben Aziza, L. Ferlazzo, C. Naylor, A. Balan, A. T. C. Johnson Jr. and R. Braive, *ACS Nano*, 2018, **12**, 3235–3242.

26 A. K. Geim and K. S. Novoselov, in *Nanoscience and technology: a collection of reviews from nature journals*, World Scientific, 2010, pp. 11–19.

27 F. Schedin, A. K. Geim, S. V. Morozov, E. W. Hill, P. Blake, M. I. Katsnelson and K. S. Novoselov, *Nat. Mater.*, 2007, **6**, 652–655.

28 B. Chakraborty, A. Bera, D. V. S. Muthu, S. Bhowmick, U. V. Waghmare and A. K. Sood, *Phys. Rev. B: Condens. Matter Mater. Phys.*, 2012, **85**, 161403.

29 A. Armano, G. Buscarino, M. Cannas, F. M. Gelardi, F. Giannazzo, E. Schilirò and S. Agnello, *Carbon*, 2018, **127**, 270–279.

30 J. Vejpravova, B. Pacakova, J. Endres, A. Mantlikova, T. Verhagen, V. Vales, O. Frank and M. Kalbac, *Sci. Rep.*, 2015, **5**, 1–9.

31 T. Vincent, V. Panchal, T. Booth, S. R. Power, A.-P. Jauho, V. Antonov and O. Kazakova, *2D Mater.*, 2018, **6**, 015022.

32 Z. Peng, X. Chen, Y. Fan, D. J. Srolovitz and D. Lei, *Light: Sci. Appl.*, 2020, **9**, 1–25.

33 W. Bao, X. Cai, D. Kim, K. Sridhara and M. S. Fuhrer, *Appl. Phys. Lett.*, 2013, **102**, 042104.

34 U. Lee, Y. Han, S. Lee, J. S. Kim, Y. H. Lee, U. J. Kim and H. Son, *ACS Nano*, 2019, **14**, 919–926.

35 R. Rao, A. E. Islam, S. Singh, R. Berry, R. K. Kawakami, B. Maruyama and J. Katoch, *Phys. Rev. B*, 2019, **99**, 195401.

36 G. Paolicelli, M. Tripathi, V. Corradini, A. Candini and S. Valeri, *Nanotechnology*, 2015, **26**, 055703.

37 G. Chilkoor, N. Shrestha, A. Kutana, M. Tripathi, F. C. Robles Hernández, B. I. Yakobson, M. Meyyappan, A. B. Dalton, P. M. Ajayan and M. M. Rahman, *ACS Nano*, 2020, **15**, 447–454.

38 D.-H. Cho, L. Wang, J.-S. Kim, G.-H. Lee, E. S. Kim, S. Lee, S. Y. Lee, J. Hone and C. Lee, *Nanoscale*, 2013, **5**, 3063–3069.

39 N. Levy, S. A. Burke, K. L. Meaker, M. Panlasigui, A. Zettl, F. Guinea, A. H. C. Neto and M. F. Crommie, *Science*, 2010, **329**, 544–547.

40 V. M. Pereira and A. H. C. Neto, *Phys. Rev. Lett.*, 2009, **103**, 046801.

41 Q. H. Wang, Z. Jin, K. K. Kim, A. J. Hilmer, G. L. C. Paulus, C.-J. Shih, M.-H. Ham, J. D. Sanchez-Yamagishi, K. Watanabe and T. Taniguchi, *Nat. Chem.*, 2012, **4**, 724–732.

42 C. Lee, X. Wei, J. W. Kysar and J. Hone, *science*, 2008, **321**, 385–388.

43 J. Xue, J. Sanchez-Yamagishi, D. Bulmash, P. Jacquod, A. Deshpande, K. Watanabe, T. Taniguchi, P. Jarillo-Herrero and B. J. LeRoy, *Nat. Mater.*, 2011, **10**, 282–285.

44 B. Amorim, A. Cortijo, F. De Juan, A. G. Grushin, F. Guinea, A. Gutiérrez-Rubio, H. Ochoa, V. Parente, R. Roldán and P. San-Jose, *Phys. Rep.*, 2016, **617**, 1–54.

45 L. Dou, A. B. Wong, Y. Yu, M. Lai, N. Kornienko, S. W. Eaton, A. Fu, C. G. Bischak, J. Ma and T. Ding, *Science*, 2015, **349**, 1518–1521.

46 A. Molle, J. Goldberger, M. Houssa, Y. Xu, S.-C. Zhang and D. Akinwande, *Nat. Mater.*, 2017, **16**, 163–169.

47 N. Ferralis, *J. Mater. Sci.*, 2010, **45**, 5135–5149.

48 H. J. Conley, B. Wang, J. I. Ziegler, R. F. Haglund Jr., S. T. Pantelides and K. I. Bolotin, *Nano Lett.*, 2013, **13**, 3626–3630.

49 H. Li, A. W. Contryman, X. Qian, S. M. Ardakani, Y. Gong, X. Wang, J. M. Weisse, C. H. Lee, J. Zhao and P. M. Ajayan, *Nat. Commun.*, 2015, **6**, 1–7.

50 K. S. Novoselov, A. K. Geim, S. V. Morozov, D.-e. Jiang, Y. Zhang, S. V. Dubonos, I. V. Grigorieva and A. A. Firsov, *Science*, 2004, **306**, 666–669.

51 B. Radisavljevic, A. Radenovic, J. Brivio, V. Giacometti and A. Kis, *Nat. Nanotechnol.*, 2011, **6**, 147–150.

52 F. Schwierz, *Nat. Nanotechnol.*, 2010, **5**, 487–496.

53 L. Gomez, I. Aberg and J. L. Hoyt, *IEEE Electron Device Lett.*, 2007, **28**, 285–287.

54 A. C. Ferrari, J. C. Meyer, V. Scardaci, C. Casiraghi, M. Lazzeri, F. Mauri, S. Piscanec, D. Jiang, K. S. Novoselov and S. Roth, *Phys. Rev. Lett.*, 2006, **97**, 187401.

55 S. Pisana, M. Lazzeri, C. Casiraghi, K. S. Novoselov, A. K. Geim, A. C. Ferrari and F. Mauri, *Nat. Mater.*, 2007, **6**, 198–201.

56 X. Lu, M. I. B. Utama, X. Wang, W. Xu, W. Zhao, M. H. S. Owen and Q. Xiong, *Small*, 2017, **13**, 1701039.

57 E. Lorchat, G. Froehlicher and S. Berciaud, *ACS Nano*, 2016, **10**, 2752–2760.

58 B. R. Carvalho, L. M. Malard, J. M. Alves, C. Fantini and M. A. Pimenta, *Phys. Rev. Lett.*, 2015, **114**, 136403.

59 C. K. Maiti, *Solid-State Electron.*, 2004, **8**, 1255.

60 S. Piscanec, M. Lazzeri, F. Mauri, A. C. Ferrari and J. Robertson, *Phys. Rev. Lett.*, 2004, **93**, 185503.

61 J. Maultzsch, S. Reich, C. Thomsen, H. Requardt and P. Ordejón, *Phys. Rev. Lett.*, 2004, **92**, 075501.

62 Y.-R. Lee, J.-X. Huang, J.-C. Lin and J.-R. Lee, *J. Phys. Chem. C*, 2017, **121**, 27427–27436.

63 Y. C. Cheng, Z. Y. Zhu, G. S. Huang and U. Schwingenschlögl, *Phys. Rev. B: Condens. Matter Mater. Phys.*, 2011, **83**, 115449.

64 S. Piscanec, M. Lazzeri, J. Robertson, A. C. Ferrari and F. Mauri, *Phys. Rev. B: Condens. Matter Mater. Phys.*, 2007, **75**, 035427.

65 S. Ryu, L. Liu, S. Berciaud, Y.-J. Yu, H. Liu, P. Kim, G. W. Flynn and L. E. Brus, *Nano Lett.*, 2010, **10**, 4944–4951.

66 C. Casiraghi, S. Pisana, K. S. Novoselov, A. K. Geim and A. C. Ferrari, *Appl. Phys. Lett.*, 2007, **91**, 233108.

67 J. E. Lee, G. Ahn, J. Shim, Y. S. Lee and S. Ryu, *Nat. Commun.*, 2012, **3**, 1–8.

68 M. Tripathi, A. King, G. Fratta, M. Meloni, M. Large, J. P. Salvage, N. M. Pugno and A. B. Dalton, *ACS Omega*, 2018, **3**, 17000–17009.

69 A. Michail, N. Delikoukos, J. Parthenios, C. Galiotis and K. Papagelis, *Appl. Phys. Lett.*, 2016, **108**, 173102.

70 Y. Wang, C. Cong, C. Qiu and T. Yu, *Small*, 2013, **9**, 2857–2861.

71 J. E. Proctor, E. Gregoryanz, K. S. Novoselov, M. Lotya, J. N. Coleman and M. P. Halsall, *Phys. Rev. B: Condens. Matter Mater. Phys.*, 2009, **80**, 073408.

72 F. Ding, H. Ji, Y. Chen, A. Herklotz, K. Dörr, Y. Mei, A. Rastelli and O. G. Schmidt, *Nano Lett.*, 2010, **10**, 3453–3458.

73 J. Zabel, R. R. Nair, A. Ott, T. Georgiou, A. K. Geim, K. S. Novoselov and C. Casiraghi, *Nano Lett.*, 2012, **12**, 617–621.

74 C. Metzger, S. Rémi, M. Liu, S. V. Kusminskiy, A. H. Castro Neto, A. K. Swan and B. B. Goldberg, *Nano Lett.*, 2010, **10**, 6–10.

75 T. Jiang, Z. Wang, X. Ruan and Y. Zhu, *2D Mater.*, 2018, **6**, 015026.

76 C. Rice, R. J. Young, R. Zan, U. Bangert, D. Wolverson, T. Georgiou, R. Jalil and K. S. Novoselov, *Phys. Rev. B: Condens. Matter Mater. Phys.*, 2013, **87**, 081307.

77 M. Tripathi, R. Garriga, F. Lee, S. P. Ogilvie, A. A. Graf, M. Large, P. Lynch, K. Papagelis, J. N. Parthenios and V. L. Cebolla, *2D Mater.*, 2022, **9**, 045033.

78 Z. Lin, W. Liu, S. Tian, K. Zhu, Y. Huang and Y. Yang, *Sci. Rep.*, 2021, **11**, 1–9.

79 T. Verhagen, V. Vales, O. Frank, M. Kalbac and J. Vejpravova, *Carbon*, 2017, **119**, 483–491.

80 D. Yoon, Y.-W. Son and H. Cheong, *Nano Lett.*, 2011, **11**, 3227–3231.

81 W. Chen, X. Gui, L. Yang, H. Zhu and Z. Tang, *Nanoscale Horiz.*, 2019, **4**, 291–320.

82 J. H. Lee, A. Avsar, J. Jung, J. Y. Tan, K. Watanabe, T. Taniguchi, S. Natarajan, G. Eda, S. Adam and A. H. Castro Neto, *Nano Lett.*, 2015, **15**, 319–325.

83 S. Schumacher, T. O. Wehling, P. Lazic, S. Runte, D. F. Förster, C. Busse, M. Petrovic, M. Kralj, S. Blügel and N. Atodiresei, *Nano Lett.*, 2013, **13**, 5013–5019.

84 P. L. Levesque, S. S. Sabri, C. M. Aguirre, J. Guillemette, M. Siaj, P. Desjardins, T. Szkopek and R. Martel, *Nano Lett.*, 2011, **11**, 132–137.

85 H. Xu, Y. Chen, J. Zhang and H. Zhang, *Small*, 2012, **8**, 2833–2840.

86 F. R. Bagsican, A. Winchester, S. Ghosh, X. Zhang, L. Ma, M. Wang, H. Murakami, S. Talapatra, R. Vajtai and P. M. Ajayan, *Sci. Rep.*, 2017, **7**, 1–10.

87 A. Piazza, F. Giannazzo, G. Buscarino, G. Fisichella, A. La Magna, F. Roccaforte, M. Cannas, F. M. Gelardi and S. Agnello, *Phys. Status Solidi A*, 2016, **213**, 2341–2344.

88 J. Zhang, J. Xiao, X. Meng, C. Monroe, Y. Huang and J.-M. Zuo, *Phys. Rev. Lett.*, 2010, **104**, 166805.

89 K. Zhang and M. Arroyo, *J. Appl. Phys.*, 2013, **113**, 193501.

90 W. Zhu, T. Low, V. Perebeinos, A. A. Bol, Y. Zhu, H. Yan, J. Tersoff and P. Avouris, *Nano Lett.*, 2012, **12**, 3431–3436.

91 T. Verhagen, B. Pacakova, M. Bousa, U. Hübner, M. Kalbac, J. Vejpravova and O. Frank, *Sci. Rep.*, 2019, **9**, 1–7.

92 F. Long, P. Yasaei, R. Sanoj, W. Yao, P. Král, A. Salehi-Khojin and R. Shahbazian-Yassar, *ACS Appl. Mater. Interfaces*, 2016, **8**, 18360–18366.

93 A. A. Graf, S. P. Ogilvie, H. J. Wood, C. J. Brown, M. Tripathi, A. A. K. King, A. B. Dalton and M. J. Large, *Chem. Mater.*, 2020, **32**, 6213–6221.

94 V. P. Gupta, *Molecular and Laser Spectroscopy*, 2022, DOI: **10.1016/C2020-0-03784-9**.

95 M. Hosseini, M. Elahi, M. Pourfath and D. Esseni, *IEEE Trans. Electron Devices*, 2015, **62**, 3192–3198.

96 Z. Liu, M. Amani, S. Najmaei, Q. Xu, X. Zou, W. Zhou, T. Yu, C. Qiu, A. G. Birdwell and F. J. Crowne, *Nat. Commun.*, 2014, **5**, 1–9.

97 S. H. Choi, Y. J. Kim, W. Yang and K. K. Kim, *J. Korean Phys. Soc.*, 2019, **74**, 1032–1038.

98 Y. Zhang, M. Heiranian, B. Janicek, Z. Budrikis, S. Zapperi, P. Y. Huang, H. T. Johnson, N. R. Aluru, J. W. Lyding and N. Mason, *Nano Lett.*, 2018, **18**, 2098–2104.

99 I. Meric, M. Y. Han, A. F. Young, B. Ozyilmaz, P. Kim and K. L. Shepard, *Nat. Nanotechnol.*, 2008, **3**, 654–659.

100 L. Britnell, R. V. Gorbachev, R. Jalil, B. D. Belle, F. Schedin, A. Mishchenko, T. Georgiou, M. I. Katsnelson, L. Eaves and S. V. Morozov, *Science*, 2012, **335**, 947–950.

101 K. S. Novoselov, O. A. Mishchenko, O. A. Carvalho and A. H. Castro Neto, *Science*, 2016, **353**, aac9439.

102 L. T. Zhuravlev, *Colloids Surf., A*, 2000, **173**, 1–38.

103 L. Liu, S. Ryu, M. R. Tomasik, E. Stolyarova, N. Jung, M. S. Hybertsen, M. L. Steigerwald, L. E. Brus and G. W. Flynn, *Nano Lett.*, 2008, **8**, 1965–1970.

104 W. G. Cullen, M. Yamamoto, K. M. Burson, J.-H. Chen, C. Jang, L. Li, M. S. Fuhrer and E. D. Williams, *Phys. Rev. Lett.*, 2010, **105**, 215504.

105 N. M. R. Peres, *Rev. Mod. Phys.*, 2010, **82**, 2673.

106 S. D. Sarma, S. Adam, E. H. Hwang and E. Rossi, *Rev. Mod. Phys.*, 2011, **83**, 407.

107 R. V. Gorbachev, I. Riaz, R. R. Nair, R. Jalil, L. Britnell, B. D. Belle, E. W. Hill, K. S. Novoselov, K. Watanabe and T. Taniguchi, *Small*, 2011, **7**, 465–468.

108 W. Bao, F. Miao, Z. Chen, H. Zhang, W. Jang, C. Dames and C. N. Lau, *Nat. Nanotechnol.*, 2009, **4**, 562–566.

109 M. Yankowitz, K. Watanabe, T. Taniguchi, P. San-Jose and B. J. LeRoy, *Nat. Commun.*, 2016, **7**, 1–8.

110 F. Zheng, K.-i. Sasaki, R. Saito, W. Duan and B.-L. Gu, *J. Phys. Soc. Jpn.*, 2009, **78**, 074713.

111 W. Zhang, C.-P. Chuu, J.-K. Huang, C.-H. Chen, M.-L. Tsai, Y.-H. Chang, C.-T. Liang, Y.-Z. Chen, Y.-L. Chueh and J.-H. He, *Sci. Rep.*, 2014, **4**, 1–8.

112 W. J. Yu, Y. Liu, H. Zhou, A. Yin, Z. Li, Y. Huang and X. Duan, *Nat. Nanotechnol.*, 2013, **8**, 952–958.

113 T. Georgiou, R. Jalil, B. D. Belle, L. Britnell, R. V. Gorbachev, S. V. Morozov, Y.-J. Kim, A. Gholinia, S. J. Haigh and O. Makarovsky, *Nat. Nanotechnol.*, 2013, **8**, 100–103.

114 W. H. Chae, J. D. Cain, E. D. Hanson, A. A. Murthy and V. P. Dravid, *Appl. Phys. Lett.*, 2017, **111**, 143106.

115 A. Tiberj, M. Rubio-Roy, M. Paillet, J. R. Huntzinger, P. Landois, M. Mikolasek, S. Contreras, J. L. Sauvajol, E. Dujardin and A. A. Zahab, *Sci. Rep.*, 2013, **3**, 1–6.

116 T. Gong, J. Zhang, Y. Zhu, X. Wang, X. Zhang and J. Zhang, *Carbon*, 2016, **102**, 245–254.

117 Z. Yan, J. Lin, Z. Peng, Z. Sun, Y. Zhu, L. Li, C. Xiang, E. L. Samuel, C. Kittrell and J. M. Tour, *ACS Nano*, 2012, **6**, 9110–9117.

118 R. He, L. Zhao, N. Petrone, K. S. Kim, M. Roth, J. Hone, P. Kim, A. Pasupathy and A. Pinczuk, *Nano Lett.*, 2012, **12**, 2408–2413.

119 S. J. Chae, F. Güneş, K. K. Kim, E. S. Kim, G. H. Han, S. M. Kim, H. J. Shin, S. M. Yoon, J. Y. Choi and M. H. Park, *Adv. Mater.*, 2009, **21**, 2328–2333.

120 R. Van Gastel, A. J. Martínez-Galera, J. Coraux, H. Hattab, D. Wall, F.-J. M. Zu Heringdorf, M. Horn-von Hoegen, J. M. Gómez-Rodríguez, B. Poelsema and C. Busse, *New J. Phys.*, 2009, **11**, 113056.

121 H. Mei, R. Huang, J. Y. Chung, C. M. Stafford and H.-H. Yu, *Appl. Phys. Lett.*, 2007, **90**, 151902.

122 H.-H. Yu and J. W. Hutchinson, *Int. J. Fract.*, 2002, **113**, 39–55.

123 B. Pacakova, J. Vejpravova, A. Repko, A. Mantlikova and M. Kalbac, *Carbon*, 2015, **95**, 573–579.

124 R. Wu, L. Gan, X. Ou, Q. Zhang and Z. Luo, *Carbon*, 2016, **98**, 138–143.

125 D. Luo, X. You, B.-W. Li, X. Chen, H. J. Park, M. Jung, T. Y. Ko, K. Wong, M. Yousaf and X. Chen, *Chem. Mater.*, 2017, **29**, 4546–4556.

126 J. Kwak, Y. Jo, S.-D. Park, N. Y. Kim, S.-Y. Kim, H.-J. Shin, Z. Lee, S. Y. Kim and S.-Y. Kwon, *Nat. Commun.*, 2017, **8**, 1–12.

127 M. Nolan and S. D. Elliott, *Phys. Chem. Chem. Phys.*, 2006, **8**, 5350–5358.

128 Y. Yang, Z. Lin, R. Li, Y. Li, W. Liu, S. Tian, K. Zhu and L. Long, *Microstructures*, 2021, **1**, 2021002.

129 J. J. Bae, H. Y. Jeong, G. H. Han, J. Kim, H. Kim, M. S. Kim, B. H. Moon, S. C. Lim and Y. H. Lee, *Nanoscale*, 2017, **9**, 2541–2547.

130 S. Sahoo, A. P. S. Gaur, M. Ahmadi, M. J. F. Guinel and R. S. Katiyar, *J. Phys. Chem. C*, 2013, **117**, 9042–9047.

131 N. Bonini, M. Lazzeri, N. Marzari and F. Mauri, *Phys. Rev. Lett.*, 2007, **99**, 176802.

132 I. Calizo, A. A. Balandin, W. Bao, F. Miao and C. N. Lau, *Nano Lett.*, 2007, **7**, 2645–2649.

133 A. T. Apostolov, I. N. Apostolova and J. M. Wesselinowa, *J. Phys.: Condens. Matter*, 2012, **24**, 235401.

134 S. Pak, J. Lee, A. R. Jang, S. Kim, K. H. Park, J. I. Sohn and S. Cha, *Adv. Funct. Mater.*, 2020, **30**, 2002023.